POLITECNICO DI TORINO
Repository ISTITUZIONALE

Tuning g-C3N4 photocatalysts via precursor selection: Impact on pollutant degradation and N2 fixation

Original
Tuning g-C3N4 photocatalysts via precursor selection: Impact on pollutant degradation and N2 fixation / Pathak, M., Vaiano, V., Venditto, V., Esposito, S., Castellino, M., Daniel, C., Sacco, O.. - In: JOURNAL OF PHOTOCHEMISTRY AND PHOTOBIOLOGY. A, CHEMISTRY. - ISSN 1010-6030. - 485:1(2027), pp. 1-18. [10.1016/j.jphotochem.2026.117819]

Availability:
This version is available at: 11583/3017768 since: 2026-11-11T14:35:43Z

Publisher:
Elsevier

Published
DOI:10.1016/j.jphotochem.2026.117819

Terms of use:

This article is made available under terms and conditions as specified in the corresponding bibliographic description in the repository

Publisher copyright

(Article begins on next page)

29 November 2026

Journal of Photochemistry & Photobiology, A: Chemistry 485 (2027) 117819

Contents lists available at ScienceDirect

Journal of Photochemistry & Photobiology, A: Chemistry

journal homepage: www.elsevier.com/locate/jphotochem

Tuning g-C_3N_4 photocatalysts via precursor selection: Impact on pollutant degradation and N_2 fixation

Mohit Pathak [a,*], Vincenzo Vaiano [b], Vincenzo Venditto [a], Serena Esposito [c,*], Micaela Castellino [c,d], Christophe Daniel [a], Olga Sacco [a]

[a] Department of Chemistry and Biology "A. Zambelli" and INSTM Unit of Salerno, University of Salerno, Via Giovanni Paolo II, 132, 84084 Fisciano, (SA), Italy
[b] Department of Industrial Engineering, University of Salerno, Via Giovanni Paolo II 132, 84084 Fisciano, (SA), Italy
[c] Department of Applied Science and Technology and INSTM Unit of Torino - Politecnico, Politecnico di Torino, Corso Duca degli Abruzzi 24, 10129 Torino, Italy
[d] Center for Sustainable Future Technologies, Istituto Italiano di Tecnologia, Via Livorno 60, 10144 Torino, Italy

ARTICLE INFO

Keywords:
G-C_3N_4
Precursor effect
Chloramphenicol
Atrazine
Nitrogen fixation
Visible-light-driven
Photocatalysis
Environmental remediation

ABSTRACT

Water scarcity and contamination demand multifunctional photocatalysts capable of addressing both pollutant removal and sustainable nutrient production. In this work, graphitic carbon nitride (g-C_3N_4) synthesized from urea and melamine was systematically investigated to establish precursor-dependent structure-property-performance relationships governing photocatalytic pollutant degradation and nitrogen fixation. Comprehensive structural, morphological, surface, and optical characterization revealed that precursor selection significantly influences the physicochemical properties of g-C_3N_4. The urea-derived material exhibited a porous tubular morphology and a higher specific surface area (41 $m^2\ g^{-1}$), which favored chloramphenicol adsorption (≈60% during the dark stage) and resulted in superior photocatalytic degradation (92% under UV irradiation). In contrast, the melamine-derived sample displayed a more ordered polymeric framework, enhanced visible-light absorption, a narrower optical band gap, and distinct surface nitrogen chemical environments, which may collectively contribute to its improved performance in photocatalytic N_2 fixation. As a result, ammonia production reached 27 μmol $g^{-1}\ h^{-1}$ in water and increased to 162.33 μmol $g^{-1}\ h^{-1}$ in the presence of ethanol as a hole scavenger. These findings demonstrate that different photocatalytic reactions are influenced by distinct combinations of material properties, highlighting precursor-dependent, reaction-specific performance: the urea-derived g-C3N4 favors chloramphenicol removal through its higher adsorption capacity, whereas the melamine-derived material exhibits superior performance in photocatalytic nitrogen fixation. Overall, this work demonstrates that precursor selection is a simple yet effective strategy for tailoring the physicochemical properties of g-C_3N_4 toward specific photocatalytic functions and establishes a unified structure-property-performance framework for the rational design of multifunctional photocatalysts for environmental remediation and sustainable ammonia production.

1. Introduction

Water scarcity and contamination represent critical challenges for environmental sustainability and agricultural productivity [1]. Only a limited fraction of global water resources is available as freshwater, and its quality is increasingly compromised by the continuous release of pollutants such as pharmaceuticals, pesticides, heavy metals, dyes, and microplastics into aquatic environments [2–7]. Moreover, the widespread use of untreated or poorly treated wastewater for irrigation further threatens both crop productivity and human health [8,9]. At the same time, the increasing demand for essential nutrients, particularly nitrogen, for agricultural applications highlights the need for sustainable nutrient management strategies [10]. In this context, the development of technologies capable of simultaneously addressing water purification and nutrient recovery is highly desirable.

Photocatalysis has emerged as a promising and sustainable approach, as it can exploit solar energy to degrade organic pollutants while enabling valuable chemical transformations such as nitrogen fixation under mild conditions, without generating harmful byproducts [11–14]. In particular, the integration of pollutant degradation with

* Corresponding authors.
E-mail addresses: mpathak@unisa.it (M. Pathak), serena_esposito@polito.it (S. Esposito).

https://doi.org/10.1016/j.jphotochem.2026.117819
Received 1 September 2026; Received in revised form 22 October 2026; Accepted 22 October 2026
Available online 27 October 2026
1010-6030/© 2026 The Authors. Published by Elsevier B.V. This is an open access article under the CC BY license (http://creativecommons.org/licenses/by/4.0/).

photocatalytic N_2 fixation represents an attractive yet still underexplored strategy for achieving dual environmental and agricultural benefits [15].

Among the various photocatalytic materials, graphitic carbon nitride (g-C_3N_4) has attracted significant attention due to its metal-free nature, suitable band gap, chemical stability, and versatility in environmental and energy-related applications [16,17]. Since its first report as a polymeric semiconductor, g-C_3N_4 has been widely investigated for applications including pollutant degradation, hydrogen evolution, CO_2 reduction, and nitrogen fixation [13,18–24]. A key advantage of g-C_3N_4 lies in its structural tunability, which can be effectively modulated through the choice of nitrogen-rich precursors and synthesis conditions [25–27]. Although different precursors can yield materials with the same nominal composition, their distinct condensation pathways lead to significant variations in morphology, porosity, surface functional groups, and electronic structure, ultimately affecting photocatalytic performance.

Recent literature has continued to probe how urea- and melamine-based precursors dictate the structure and reactivity of g-C_3N_4, though largely within single-reaction frameworks rather than across mechanistically distinct photocatalytic pathways. Briševac et al. (2025) systematically compared g-C_3N_4 derived from urea, melamine, and melamine/cyanuric-acid supramolecular precursors for procaine degradation, and reported that morphology and porosity - rather than precursor identity alone -were the dominant descriptors of activity, with loosely stacked, porous architectures outperforming denser aggregates [28]. Negro (2024) examined a continuous urea/melamine ratio series and found that increasing the urea fraction progressively favored thinner, more exfoliated nanosheet morphologies with higher surface area, culminating in a carbon-rich U80-C_3N_4 (64.8 $m^2\ g^{-1}$) that achieved the methylene blue degradation performance among the series, attributing this to enhanced light harvesting and charge-carrier transport in the exfoliated structure [29]. Similarly, a 2025 study on simultaneous melamine/urea polycondensation reported that urea-rich formulations (90:10 urea:melamine) produced highly exfoliated, spider-web-like nanosheets with the highest surface area and the best photocatalytic performance for tetracycline removal, again identifying superoxide-radical-mediated oxidation as the dominant pathway [30]. In a related comparison of six carbon-nitride precursors for peroxide activation, urea-derived g-C_3N_4 was distinguished not by its surface area but by the widest optical band gap and the most positive valence-band potential among the precursor set, which was linked to its superior oxidizing capability toward pollutants [27].

Despite extensive studies on g-C_3N_4, a systematic understanding of how precursor-dependent structural features govern multifunctional photocatalytic processes-particularly the interplay between pollutant degradation and nitrogen fixation-remains limited. Most reported studies focus on either pollutant degradation or N_2 fixation independently, while the relationship between adsorption properties, defect chemistry (e.g., nitrogen vacancies), and charge carrier dynamics across these coupled processes is still not fully clarified.

Herein, graphitic carbon nitride (g-C_3N_4) photocatalysts synthesized from two different nitrogen-rich precursors, melamine and urea, are systematically investigated to elucidate how precursor selection influences the structure-property-performance relationships governing photocatalytic pollutant degradation and nitrogen fixation. The materials are evaluated for the degradation of chloramphenicol and atrazine under light irradiation, as well as for photocatalytic N_2 fixation. Although precursor-dependent modifications of the physicochemical properties of g-C_3N_4 have been widely reported, their influence on the performance of different photocatalytic reactions remains insufficiently understood. In particular, the respective contributions of morphology, porosity, surface chemistry, and electronic properties to adsorption-related and charge-transfer-related processes require further clarification.

This study aims to establish structure-property-performance relationships by correlating the physicochemical characteristics of precursor-derived g-C_3N_4 with its photocatalytic behavior across reactions involving different processes. By comparing pollutant degradation and nitrogen fixation within a consistent experimental framework for each reaction, this work investigates how precursor-dependent material properties influence photocatalytic performance. Few studies have systematically discriminated adsorption-controlled versus charge-transfer-driven photocatalytic pathways for g-C_3N_4 derived from different precursors under unified experimental conditions. By addressing this knowledge gap, the present study provides comparative insights into precursor-dependent photocatalytic behavior and the potential for tailoring g-C_3N_4 materials for environmental remediation and sustainable ammonia production.

2. Experiment section

2.1. Materials

Melamine ($C_3H_6N_6$) and urea (CH_4N_2O) were purchased from Sigma-Aldrich and used as received without further purification. The model pollutants chloramphenicol (CAP) and atrazine (ATZ) were also obtained from Sigma-Aldrich. All chemicals were of analytical grade and used without additional purification. Deionized water was used throughout all experiments.

2.2. Preparation method

Graphitic carbon nitride (g-C_3N_4) was synthesized via thermal polycondensation of nitrogen-rich precursors, namely melamine and urea. All thermal treatments were carried out in a conventional muffle furnace under static ambient air, without any controlled gas flow.

2.2.1. Synthesis of g-C_3N_4 from melamine

8 g of melamine were accurately weighed and placed in a high-temperature-resistant placed in a ceramic crucible covered with a lid. The crucible was transferred to a muffle furnace and heated in static ambient air at a rate of 5 °C min^{-1} up to 500 °C, where the temperature was maintained for 2 h. After natural cooling to room temperature, the obtained pale-orange solid was washed three times with 0.1 M nitric acid, dried overnight at 80 °C, and ground into a fine powder. The resulting material was stored in labelled vials for further use.

2.2.2. Synthesis of g-C_3N_4 from urea

30 g of urea were accurately weighed and placed in a a ceramic crucible covered with a lid, which was then transferred to a muffle furnace. The sample was heated at a rate of 5 °C min^{-1} up to 500 °C in static ambient air and maintained at this temperature for 2 h. After natural cooling to room temperature, the obtained material was washed three times with 0.1 M nitric acid, dried overnight at 80 °C, and ground into a fine powder. The resulting product was stored in labelled vials for further use.

Since both samples were synthesized under identical static-air conditions, the differences observed in morphology, surface chemistry, and electronic properties can be primarily attributed to the different decomposition pathways of the two precursors rather than to the calcination atmosphere itself. Nevertheless, it is recognized that the gaseous environment during thermal polycondensation may influence the condensation process and defect formation in polymeric carbon nitride, as reported in the literature.

2.3. Characterization techniques

WAXD patterns were recorded using a Bruker D2 Phaser diffractometer (35 kV, 40 mA) with nickel-filtered Cu Kα radiation, operated in reflection mode. This technique was used to identify the crystalline phases of graphitic g-C_3N_4. Samples were gently pressed onto a low-

background holder to ensure uniformity. The crystallite size was calculated using the Scherrer formula based on the X-ray diffraction (XRD) data. Debye–Scherrer eq. (1):

$$D = \frac{0.9\lambda}{\beta\cos\theta} \quad (1)$$

where λ is the wavelength of the incident X-ray, θ is the Bragg diffraction angle, and β is the full width at half maximum (FWHM) of the most intense diffraction peak.

FTIR spectra were acquired on a Bruker Vertex 70 spectrometer (DTGS detector, KBr beam splitter, resolution 2.0 cm^{-1}). KBr pellets were prepared by mixing 1–2 mg of sample with 100–150 mg of dry KBr, then pressed into transparent discs. FTIR analysis provided information on molecular vibrations and verified the presence of functional groups.

TGA was conducted using a TA Instruments Q500 system under oxygen flow (10–800 °C, 10 °C min^{-1}) to evaluate the thermal stability and estimate the composition based on the decomposition of organic phases. Samples (~5–10 mg) were loaded in platinum crucibles.

SEM images were obtained using a LEO Evo 50 microscope (10 kV, 30 μA), with samples sputter-coated with ~20 nm of gold to ensure conductivity. The analysis provided insight into surface morphology and dispersion of the composite phases. Powdered samples were mounted on carbon tape attached to aluminum stubs.

TEM analyses were carried out using a JEOL 2100Plus microscope at 200 kV. Samples were dispersed in ethanol, drop-cast onto carbon-coated copper grids, and air-dried. TEM enabled direct observation of heterojunction interfaces.

UV–Vis DRS spectra of photocatalysts were analyzed using a PerkinElmer Lambda 35 UV–Vis spectrophotometer equipped with an 88-position sample holder. Reflectance spectra were recorded relative to a calibrated standard (SRS-010-99, Labsphere Inc., North Sutton, NH). The indirect band gap energies were estimated from Tauc plots using the Kubelka–Munk function, as expressed below:

$$(F(R_\infty) \bullet h\nu)^{0.5} = f(h\nu) \quad (2)$$

where:

$F(R_\infty)$ is the Kubelka-Munk function;

h is Planck's constant [J·s];

ν is the frequency of the incident light radiation [s^{-1}];

$h\nu$ is the photon energy.

Photoluminescence (PL) spectra were collected at room temperature with a Shimadzu RF-5301PC spectrofluorometric (xenon flash lamp). Approximately 50 mg of powder was used per measurement. PL analysis provided information on charge carrier recombination behavior, supporting interpretation of photocatalytic performance. The samples for the photoluminescence analyses were dispersed in chloroform by ultrasonication for 5 min. The optical band gap energy (E_g) was estimated from the photoluminescence (PL) emission spectra. The peak emission wavelength (λ) was used to calculate E_g using the eq. (2):

$$E_g = \frac{hc}{\lambda} \quad (3)$$

where: h is Planck's constant, c is the speed of light, λ is the emission peak wavelength obtained from PL spectra. It should be noted that the optical band gap estimated from the Kubelka–Munk-transformed diffuse-reflectance spectra and Tauc plots represents the primary estimate of the semiconductor optical band gap in this study. In contrast, the energy calculated from the PL emission maximum represents the photon energy associated with radiative recombination and may be influenced by the electronic states involved in emission. Therefore, the PL-derived emission energy is used to discuss the radiative recombination characteristics of the samples and is not treated as an independent determination of the fundamental optical band gap.

BET surface area was measured via nitrogen adsorption–desorption at 77 K using a Nova Quantachrome 4200e system. BET values were calculated from an 11-point isotherm. Samples (120 mg) were degassed under vacuum at 120 °C for 4 h before analysis. This data provided insights into accessible surface area and porosity, key factors for photocatalytic activity.

X-ray photoelectron spectroscopy (XPS) was performed using a PHI 5000 Versaprobe II spectrometer. A monochromatic K-alpha X-ray source (1486.6 eV) was used, along with a dual charge compensation system consisting of an electron beam and an Ar + ion source. Survey scans were collected to evaluate the presence of chemical elements in the 1200–0 eV range (Pass Energy 187 eV), while high-resolution (HR) spectra were collected in selected regions, with a Pass Energy of 23 eV, to evaluate the relative atomic concentrations (at.%) and oxidation state of each acquired element.

2.4. Photocatalytic activity tests

2.4.1. Photocatalytic set-up for pollutants degradation

Photocatalytic experiments were carried out in a cylindrical Pyrex reactor (internal diameter: 3.5 cm; height: 28 cm; total volume: 269 mL) containing 50 mL of aqueous pollutant solution (25 mg/L of chloramphenicol (CAP) or 10 mg/L of atrazine (ATZ)) and 0.5 g/L of photocatalyst. For UV-driven reactions, four external UV lamps (8 W each, λ = 365 nm) were symmetrically arranged around the reactor to ensure uniform irradiation of the liquid phase.

For visible-light-driven reactions, experiments were performed using four visible lamps (Philips; nominal power: 8 W each), emitting in the 400–750 nm range, arranged in the same configuration.

The photon flux at the reactor surface, determined by chemical actinometry and measured with a calibrated spectroradiometer (StellarNet Inc.), was approximately 25 mW cm^{-2} for UV irradiation and 26 mW cm^{-2} for visible-light irradiation. Prior to irradiation, the suspension was magnetically stirred in the dark for 180 min to establish adsorption–desorption equilibrium. During photocatalytic experiments, continuous magnetic stirring was maintained to ensure homogeneous conditions.

The reaction progress was monitored by periodically withdrawing aliquots and measuring their absorbance at 275 nm (CAP) and 224 nm (ATZ) was measured using an Agilent Varian Cary 50 Probe UV–vis spectrophotometer. The total organic carbon (TOC) of the aqueous solutions was measured using a TOC analyzer (Multi N/C 3100S, Analytik Jena), operating with an airflow of 160 Ncm^3 /min and a sample injection volume of 500 μL.

All experiments were performed in triplicate, and median values are reported.

2.4.2. Photocatalytic set-up for nitrogen fixation

Photocatalytic nitrogen fixation experiments were carried out in a cylindrical Pyrex batch reactor (internal diameter: 2.6 cm; height: 41 cm; total volume: 200 mL). Four external UV lamps (8 W each, λ = 365 nm) were symmetrically arranged around the reactor to ensure uniform irradiation of the liquid phase. The photon flux at the reactor surface, determined by chemical actinometry and measured with a calibrated spectroradiometer (StellarNet Inc.), was approximately 25 mW cm^{-2}.

A peristaltic pump (Watson Marlow, 200 rpm) was used to continuously circulate the suspension, preventing catalyst sedimentation and ensuring homogeneous mixing. Prior to irradiation, nitrogen gas (N_2) was bubbled through the suspension at a controlled flow rate of 50 Ncc min^{-1} for 30 min in the dark to achieve saturation. The reactor was then sealed, the N_2 inlet was closed, and irradiation was initiated.

Photocatalytic experiments were carried out for 4 h using a reaction mixture consisting of 75 mL of solution and 100 mg of catalyst. The reaction media included pure water, 40% (v/v) ethanol-water mixture, and an aqueous solution containing Na_2SO_3 (100 mg in 75 mL water), where ethanol and Na_2SO_3were employed as scavengers.

Prior to illumination, the suspension was stirred in the dark for 30 min to establish adsorption-desorption equilibrium. After this equilibration period, UV light was switched on to initiate the reaction. Aliquots were withdrawn at regular time intervals, and the samples were filtered through PVDF syringe filters to remove suspended catalyst particles prior to analysis. The concentration of NH_4^+ was determined using the Nessler reagent spectrophotometric method (JB7478–87) [31], and the absorbance at 420 nm was measured using an Agilent Varian Cary 50 Probe UV–Vis Spectrophotometer. The ammonia production rate was calculated by subtracting the contribution obtained during the dark (equilibrium) period from the values measured under UV irradiation.

The ammonia production rate was calculated according to:

$$rNH_4^+ = \frac{nNH_4^+}{t.m_{cat}} \quad (3)$$

where,

nNH_4^+ is the amount of produced ammonium ion (mol), t is the reaction time (h), and

m_{cat} is the catalyst mass (g).

The concentration of ammonium ions was also determined by ion chromatography (IC) using a Dionex CS12A cation-exchange column with 20 mM methanesulfonic acid as the eluent at a flow rate of 1.0 mL min^{-1}. Prior to IC analysis, ethanol-containing reaction mixtures were filtered through a 0.22 μm membrane, acidified with 0.1 M HCl to ensure complete conversion of NH_3 to NH_4^+. The sample containing 40% ethanol was first acidify using 0.1 M HCl and then subjected to rotary evaporation at 40 °C under reduced pressure to completely remove ethanol. For experiments conducted in distilled water or using Sodium sulfite (Na_2SO_3) as the sacrificial agent, the filtered samples were similarly acidified with 0.1 M HCl before IC analysis to ensure quantitative conversion of dissolved NH_3 into NH_4^+ and prevent underestimation of the total fixed nitrogen. The NH_4^+ concentration was quantified using a calibration curve prepared from standard ammonium chloride solutions (0.5–10 ppm NH_4^+), as shown in Fig. S3 of the Supporting Information. It should be noted that the Nessler colorimetric method may be affected by reducing species present in scavenger-containing reaction mixtures, including sulfite and ethanol oxidation products, potentially leading to an overestimation of the apparent NH_4^+ concentration; therefore, IC was also employed for independent quantification.

3. Results and discussion

3.1. Morphology and structure analysis

Fig. 1a-d present the FE-SEM micrographs of g-C_3N_4 (U) and g-C_3N_4 (M) at different magnifications. The two samples exhibit markedly different morphologies depending on the precursor used. While g-C_3N_4 (U) is characterized by hollow tubular nanostructures with thin walls and a crumpled surface, g-C_3N_4 (M) displays a morphology mainly composed of disordered bulk aggregates. These irregular structures are arranged in a more densely packed texture compared to that observed for g-C_3N_4 (U). Notably, a tubular morphology has been previously reported using melamine as a precursor; however, this was achieved only after multiple post-synthesis treatments, including sonication of bulk g-C_3N_4 to produce exfoliated nanosheets, followed by thermal treatment with controlled heating and rapid quenching to induce morphological transformation [32]. In contrast, In the present work, a comparable hollow tubular architecture was obtained directly from urea under the specific one-step conditions used here, without additional post-synthesis processing.

The TEM images (Fig. 1e–h) further confirm the precursor-dependent morphological differences. The urea-derived sample, g-C_3N_4 (U), exhibits a tubular and intertwined porous network, whereas g-C_3N_4 (M) consists of denser aggregates of short rod-like structures with

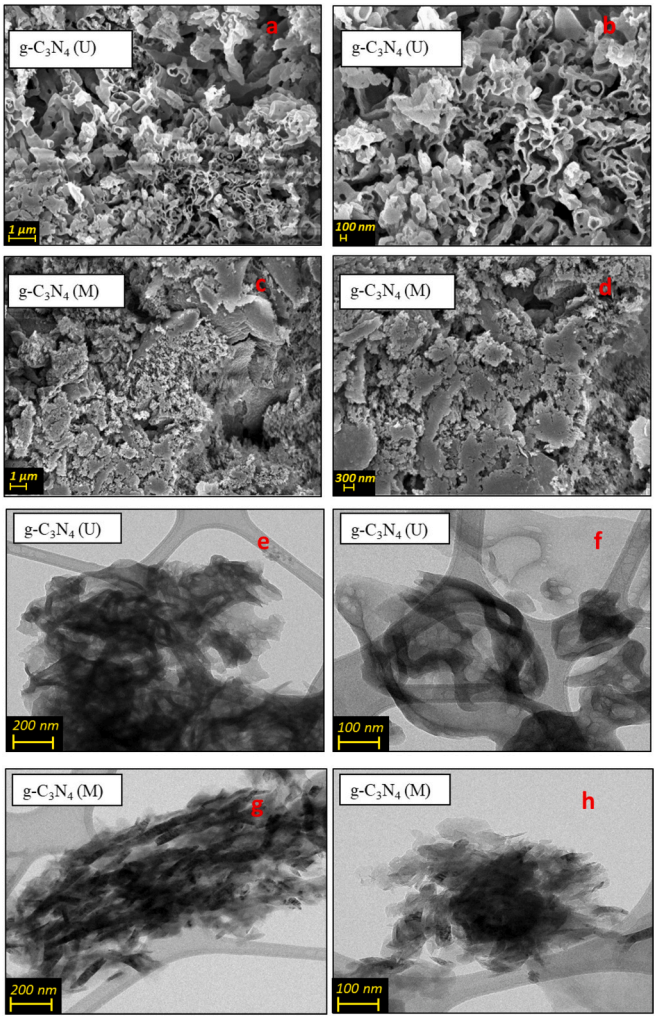

Fig. 1. FE-SEM (a-d) and high-resolution TEM images (e-h) of g-C_3N_4 (U) and g-C_3N_4 (M) samples.

reduced interparticle voids. The hollow architecture of g-C_3N_4 (U) may favor multiple light-scattering and internal-reflection phenomena, potentially improving light harvesting [33].

It should be noted, however, that the formation of tubular g-C_3N_4 cannot be attributed exclusively to the use of urea as precursor. The final morphology is likely governed by the combined effects of precursor decomposition, gas evolution, condensation kinetics, heating rate, holding time, precursor loading, calcination atmosphere, and crucible geometry. In particular, the heating rate may influence the kinetics of precursor decomposition and gas evolution, thereby affecting the formation and evolution of porous or tubular structures. Precursor loading may modify heat transfer and the local accumulation and release of gaseous decomposition products, potentially influencing the resulting morphology. Furthermore, the calcination atmosphere may affect precursor decomposition and polymer condensation through changes in the gaseous reaction environment. Indeed, Zheng et al. [34], using a broadly similar thermal polymerization route, reported a graphene-like morphology consisting of thin, platelet-like nanosheets rather than tubular structures for urea-derived g-C_3N_4. This discrepancy indicates that apparently minor differences in the thermal history and reaction environment may significantly affect the self-assembly and structural evolution of carbon nitride during pyrolysis. Therefore, the tubular morphology observed in the present work should be regarded as a feature obtained under the specific synthesis conditions adopted here, while a systematic evaluation of the individual synthesis parameters

would require a dedicated study.

The XRD patterns of the g-C_3N_4 samples synthesized are presented in Fig. 2. Both samples exhibit the two characteristic diffraction peaks of graphitic carbon nitride. The intense peak at $2\theta \approx 27.2^\circ$ corresponds to the (002) interlayer stacking reflection of the conjugated aromatic units, whereas the weaker peak at $2\theta \approx 13^\circ$ is assigned to the (100) in-plane structural packing of the repeated tri-*s*-triazine motifs, in agreement with the standard pattern of hexagonal g-C_3N_4 (JCPDS 87–1526).

Notable differences emerge when comparing the materials obtained from the two precursors. The diffraction peaks of g-C_3N_4 (U) are significantly broader and less intense than those of g-C_3N_4(M), indicating a lower degree of crystallinity and the presence of smaller structural domains. This behavior is consistent with the decomposition pathway of urea, which lacks an intrinsic *s*-triazine framework and undergoes a complex multistep pyrolysis process involving several intermediates such as biuret, cyanuric acid, ammeline and ammelide [35]. The formation of carbon nitride from such species makes it difficult to construct well-connected heptazine networks, resulting in the incorporation of structural defects within the final material. Furthermore, the high electronegativity of the oxygen atom and the strong C—O single bond in urea tend to suppress efficient condensation, leading to lower polymerization degrees compared to melamine-based synthesis [36].

In contrast, g-C_3N_4 (M) shows sharper and more defined diffraction peaks, reflecting improved structural ordering. Besides the characteristic (100) and (002) reflections, weak peaks are observed at $2\theta \approx 21$, the appearance of these reflections is typically related to the stacking of melon layers [37], a known intermediate in the thermal polymerization of melamine [38]. During the synthesis, melon species can form through stepwise condensation and subsequently undergo fusion and reconnection to yield the final graphitic carbon nitride framework explaining the presence of these additional reflections.

Overall, the XRD analysis confirms that melamine-derived carbon nitride possesses a more ordered layered structure, whereas the urea-derived counterpart contains smaller crystalline domains and a higher degree of structural imperfections. These differences in crystallinity are expected to influence the physicochemical behavior and catalytic performance of the resulting g-C_3N_4 materials.

The FT-IR spectra of both g-C_3N_4 samples (Fig. 3) display the characteristic bands of polymeric graphitic carbon nitride, confirming the successful formation of the heptazine (tri-*s*-triazine)-based framework [35]. Differences in the position and intensity of specific bands between the two samples indicate significant structural variations, which can be attributed to the distinct nature of the precursors used during synthesis.

The bands located at approximately 806 and 884 cm^{-1} are associated with the breathing modes of triazine units, confirming that the molecular structure of the prepared g-C_3N_4 is based on triazine/heptazine building blocks. In the 1200–1700 cm^{-1} region, the spectra are dominated by absorption bands corresponding to C—N stretching vibrations of aromatic heterocycles, reflecting the conjugated structure of the polymeric framework. In particular, the bands at 1630–1640 cm^{-1} and 1550–1569 cm^{-1} are attributed to N—H bending vibrations of primary amines and to stretching modes of the heptazine-derived repeating units, respectively, indicating the formation of a well-developed polymeric network.

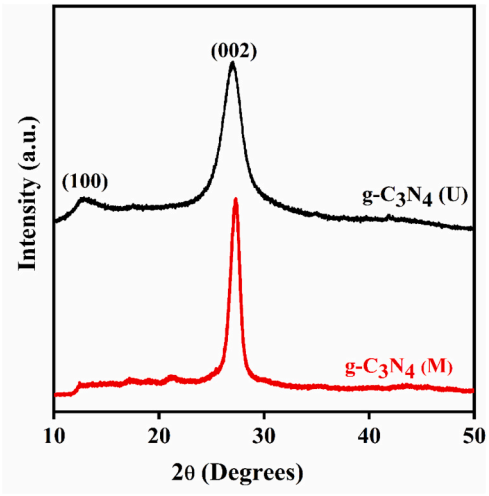

Fig. 2. XRD patterns of g-C_3N_4 (U) and g-C_3N_4 (M) samples.

Additional bands observed at 1450–1462 cm^{-1} and 1410–1412 cm^{-1} are assigned to aromatic C—N stretching vibrations, further supporting the presence of conjugated heterocyclic structures. The absorption in the 1250–1321 cm^{-1} range is indicative of bridging units, corresponding either to fully condensed C-N(—C)-C linkages or to partially condensed C-NH-C groups. Weak bands in the 2850–2957 cm^{-1} region, including those at 2925, 2957, and 2852 cm^{-1}, are associated with C—H stretching vibrations of residual -CH_2 and -CH_3 groups, suggesting the presence of incomplete condensation or surface functionalities [39].

A comparison between g-C_3N_4 (M) and g-C_3N_4 (U) reveals subtle but significant differences. While both materials retain the heptazine-based backbone, g-C_3N_4 (M) exhibits sharper and better-defined vibrational bands than g-C_3N_4 (U), suggesting a relatively more ordered polymeric framework and a higher degree of condensation. This behavior is consistent with the complex pyrolysis pathway of urea, which involves multiple intermediate species. In contrast, g-C_3N_4 (M) shows sharper and more defined peaks, reflecting a more ordered polymeric structure and a higher degree of condensation, in agreement with the direct condensation of melamine through melon intermediates [34].

To provide a semi-quantitative comparison of the polymerization degree, the integrated area ratio of the characteristic ring-breathing bands at 806 and 884 cm^{-1} to the C–N/C=N stretching region (1200–1700 cm^{-1}) was calculated. The area ratio increased from 0.057 for g-C_3N_4 (U) to 0.161 for g-C_3N_4 (M), corresponding to an approximately 2.8-fold increase. The higher relative contribution of the ring-breathing vibrations in the melamine-derived sample is consistent with a higher degree of structural condensation and polymeric ordering compared with the urea-derived g-C_3N_4.

Fig. 4 shows the thermogravimetric analysis (TGA) profiles of the two samples, g-C_3N_4 (U) and g-C_3N_4 (M), recorded under an air atmosphere. The g-C_3N_4 (M) sample exhibits a single major weight-loss event and remains thermally stable up to temperatures above 550 °C. A sharp mass loss is observed between 530 and 670 °C, which can be attributed to the oxidative decomposition of the g-C_3N_4 framework, leading to the formation of gaseous products such as CO_2 and N_2 [40].

In contrast, g-C_3N_4 (U) displays two distinct weight-loss steps. The first, occurring in the range of 25–110 °C, is associated with the removal of physisorbed water, suggesting a higher degree of surface hydration. This behavior is consistent with the presence of residual surface functional groups (e.g., -CH_2 and -CH_3), as evidenced by FTIR analysis (Fig. 3C). The second weight-loss event, observed between 450 and 615 °C, corresponds to the oxidative degradation of the carbon nitride framework to gaseous products [40].

To provide a quantitative comparison of the thermal stability and condensation degree, the residual mass at 600 °C was determined from the TGA curves. At this temperature, g-C_3N_4 (U) retained only approximately 0.5 wt% of its initial mass (99.5 wt% weight loss), whereas g-C_3N_4 (M) retained approximately 76 wt% (24 wt% weight loss). The significantly higher residual mass of g-C_3N_4 (M) demonstrates its enhanced thermal stability and greater resistance to oxidative decomposition, which is consistent with a higher degree of structural condensation and ordering, in agreement with the FTIR, XRD, and XPS analyses.

Overall, the differences in thermal behavior between the two samples reflect their distinct structural features. The broader and lower-temperature decomposition of g-C_3N_4 (U) suggests a less condensed and more defective structure, whereas the higher thermal stability of g-

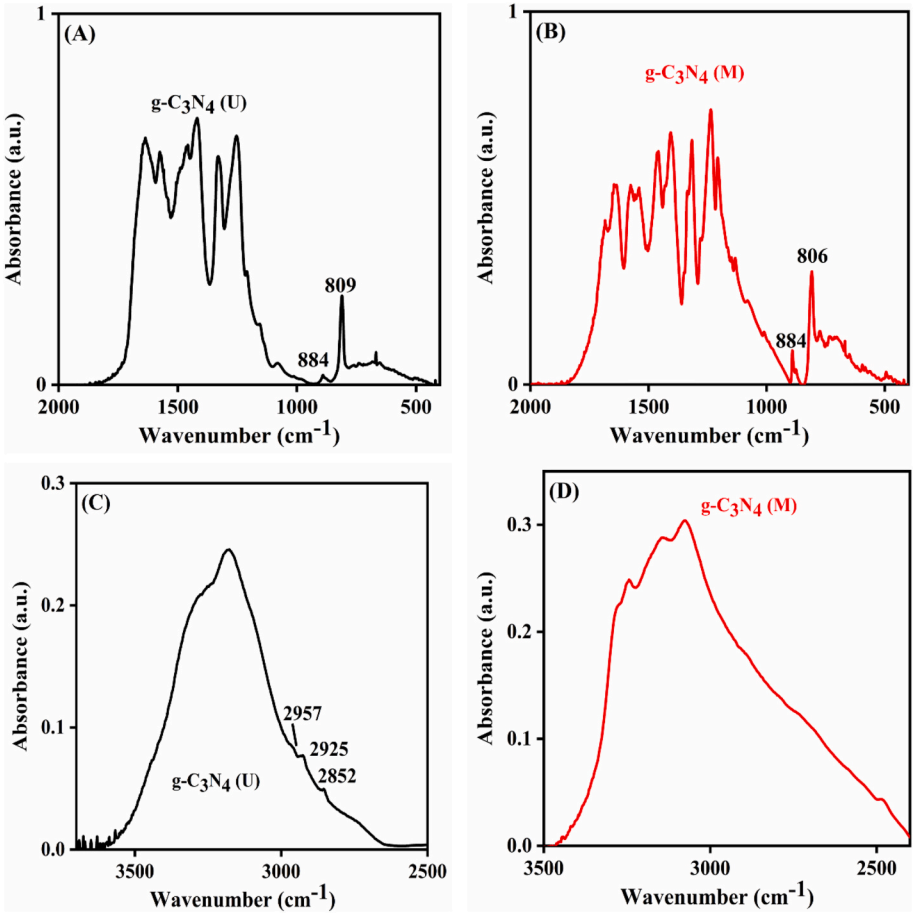

Fig. 3. FT-IR spectra in the range (A-B) 2000–400 cm^{-1} of g-C_3N_4 (U) and g-C_3N_4 (M); (C—D) 3600–2400 cm^{-1} of g-C_3N_4 (U) and g-C_3N_4 (M).

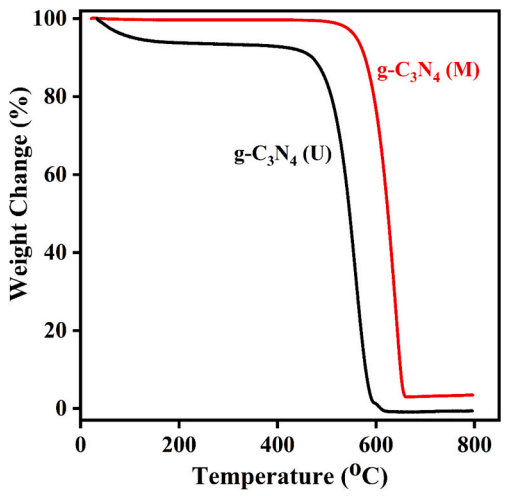

Fig. 4. TGA of g-C_3N_4 (U) and g-C_3N_4 (M) samples.

C_3N_4 (M) is indicative of a more ordered and highly polymerized network.

To gain further insight into the textural properties of the g-C_3N_4 samples, N_2 adsorption–desorption isotherms measured at −196 °C and the corresponding pore-size distribution curves were analyzed. The results are presented in Fig. 5A-B. Before analysis, 200 mg of each sample was degassed under vacuum at 120 °C for 4 h. As shown in Fig. 5A, both samples exhibit type IV adsorption–desorption isotherms, characteristic of mesoporous materials [41]. The corresponding Brunauer-Emmett-Teller (BET) specific surface areas and average pore diameters are summarized in Table 1. According to the BET analysis, g-C_3N_4 (U) exhibits a higher specific surface area (41 $m^2\ g^{-1}$) compared to g-C_3N_4 (M) (32 $m^2\ g^{-1}$), indicating a more developed porous structure. This increased surface area can be attributed to the formation of a hierarchical pore network, which enhances the accessibility of active sites and improves the interaction between the photocatalyst and reactant molecules [20].

The pore-size distribution curves (Fig. 5B) further confirm that both samples predominantly consist of mesopores, with contributions from smaller pores. Quantitative analysis of the DFT pore-size distribution revealed that the total mesopore volume of g-C_3N_4 (M) is 0.085 $cm^3\ g^{-1}$, which is higher than that of g-C_3N_4 (U) (0.072 $cm^3\ g^{-1}$). Although g-C_3N_4 (M) possesses a larger mesopore volume, g-C_3N_4 (U) exhibits a higher BET surface area. These results indicate that the textural properties of the two materials differ not only in terms of surface area but also in pore architecture. The larger mesopore volume of g-C_3N_4 (M) is expected to facilitate molecular diffusion and improve the accessibility of internal active sites, whereas the higher specific surface area of g-C_3N_4 (U) provides a greater number of accessible surface sites. Therefore, the overall adsorption behavior is expected to result from the combined effects of surface area and pore architecture rather than from a single textural parameter. In addition, the interconnected mesoporous network can facilitate reactant transport and shorten diffusion pathways, which may also contribute to charge-carrier migration during photocatalytic processes [42].

X-ray photoelectron spectroscopy (XPS) was employed to investigate the surface chemical composition and electronic structure of the as-prepared g-C_3N_4 samples. Owing to its intrinsic surface sensitivity and chemical specificity, XPS represents a powerful tool to probe the

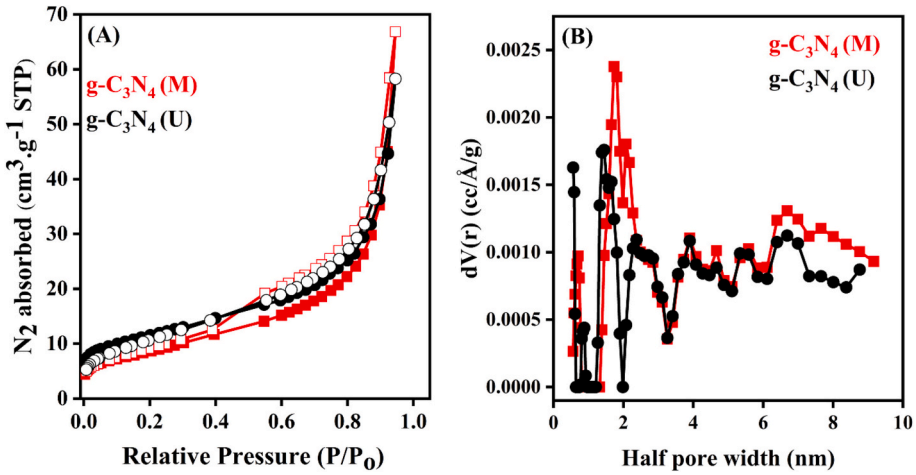

Fig. 5. A) N_2 adsorption–desorption isotherms and B) Pore size distribution of g-C_3N_4 (U) and g-C_3N_4 (M) samples.

Table 1
Brunauer-Emmett-Teller (BET) surface area, crystallite size total mesopore volume and average pore sizes for the prepared samples.

Sample	Crystallite size (nm)	Eg Tauc plot (eV)	Surface area (m^2g^{-1})	Total mesopore volume $cm^3\ g^{-1}$	Average pore sizes (nm)
g-C_3N_4 (U)	2.5	2.7	41	0.072	3–4 nm
g-C_3N_4 (M)	6.9	2.5	32	0.085	3.5–4.5 nm

Table 2
XPS data related to the relative atomic concentration (at. %) of samples: together with N1s regions deconvolution results, calculated for each of two samples.

Sample	Relative atomic concentration [at. %]			
	C1s	**O1s**		**N1s**
g-C_3N_4 (U)	42.9	2.5		54.6
g-C_3N_4 (M)	42.0	1.1		56.9
N 1 s deconvolution [%]				
	N_1 [N-C=N]	**N_2** [N-(C)$_3$]	**N_3** [H-N-C]	**N_4** [p excitons]
g-C_3N_4 (U)	65.3	17.0	12.1	5.6
g-C_3N_4 (M)	58.0	23.4	12.3	6.3

elemental composition as well as the bonding environment of carbon and nitrogen species in this class of materials. In this work, particular attention is devoted to the survey spectra, which provide an overview of the elemental composition and sample purity, and to the high-resolution C 1 s and N 1 s regions, which offer insights into the local chemical environments within the heptazine-based framework. The combined analysis of these spectral regions enables the identification of the main structural motifs and potential variations in the chemical structure, thus contributing to a deeper understanding of the material properties. The survey spectra (shown in Fig. 6) clearly display the characteristic C 1 s and N 1 s signals, while the O 1 s contribution is only barely detectable, especially in the g-C_3N_4(M). The corresponding elemental composition, expressed in terms of relative atomic concentrations, is reported in Table 2. It should be noted that these values were derived from high-resolution (HR) spectra to achieve improved energy resolution, particularly in the O 1 s regions. The Carbon-to-Nitrogen ratios are equal to 0.79 and 0.74 for g-C_3N_4(U) and g-C_3N_4(M), respectively.

A comparison of the C 1 s regions (Fig. 7) reveals the presence of three well-defined components: a contribution at approximately 284.8 eV, commonly associated with C–C/C–H bonds, a second and more intense peak at around 288.2 eV, attributed to N–C=N species within the heptazine framework, and a third feature at higher binding energy (~294 eV), assigned to π–π* shake-up transitions. A more rigorous peak fitting procedure (not shown) further suggests the presence of an additional component centred at approximately 286 eV, which will be discussed in detail later. Notably, a difference in relative

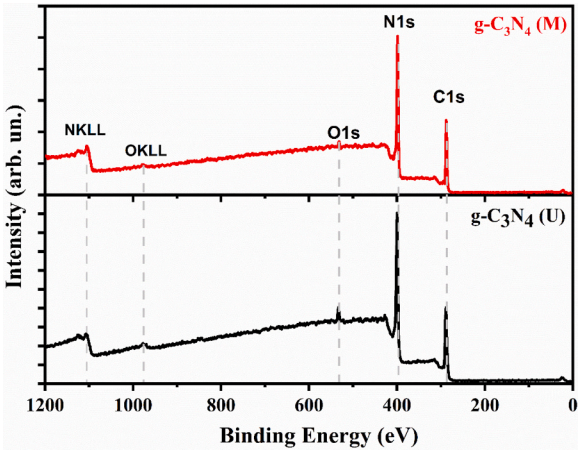

Fig. 6. XPS survey spectra for samples (from top to bottom): g-C_3N_4 (M) and g-C_3N_4 (U), respectively.

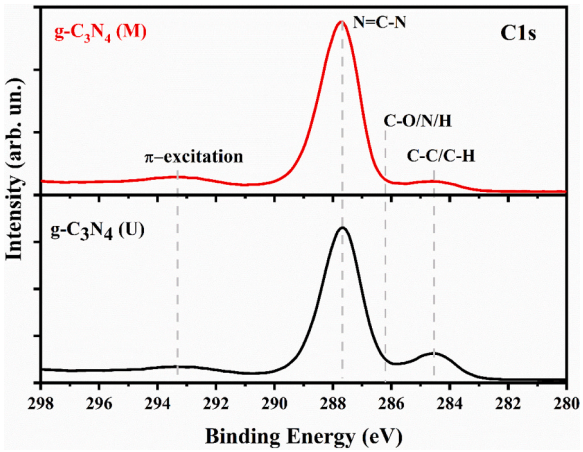

Fig. 7. XPS C1s HR spectra for samples (from top to bottom): g-C_3N_4 (M) and g-C_3N_4 (U), respectively.

intensity is observed between the two samples, particularly for the 284.8 eV contribution, which appears more pronounced in the urea-derived sample compared to the melamine-derived one. This can be the reason why the C/N ratios are different, as previously reported. If we look for an explanation for the presence of this peak at 284.8 eV in the literature, we find some sources that attribute it to adventitious carbon or graphitic carbon [43,44]. The component around 286 eV can also have multiple attributions, such as a classical C—O or C—N bond, or the presence of nitrile-type species (C≡N), which belong to the same chemical shift region. As clearly stated by V. W. Lau et al. [43], however, the latter peak significantly overlaps with the peak of adventitious carbon, so one must be careful not to overanalyse the small spectral features and not to draw too definitive conclusions. However, the presence of adventitious carbon, which usually in addition to the C—C component also carries a C—O component and sometimes even C═O (≈ 288 eV), can go hand in hand with the presence of a higher amount of O detected on the surface, in the urea-derived sample, which appears more hygroscopic, which could be due to the presence of functional groups, which can create dipolar bonds [45].

Following the analysis of the C 1 s region, the N 1 s spectra were examined to provide a detailed view of the nitrogen environments within the g-C_3N_4 framework. This high-resolution region enables the distinction of different nitrogen species, including the characteristic pyridinic and tertiary bridging nitrogen, as well as potential defect-related contributions.

The interpretation of this region, however, remains complex due to significant overlap in contributions from chemically similar nitrogen environments. In the binding energy range of approximately 398–400 eV, signals commonly attributed to the pyridine nitrogen (C=N-C) within the heptazine backbone, the bridging tertiary nitrogen (N-$(C)_3$), and defect-related species (e.g., nitrogen vacancies or under-coordinated sites) are often not easily distinguishable. The small energy separation between these components, typically on the order of ≤1 eV, introduces uncertainty in deconvolution and peak assignment. Consequently, features in this region may be subject to multiple plausible interpretations, reflecting both intrinsic structural motifs and subtle variations in the local chemical environment. These considerations highlight the importance of an accurate and consistent fitting strategy, as well as the benefit of supporting XPS analysis with complementary techniques to gain a more complete understanding of the material. Referring to the existing literature, we found several works that attempted to define the components of this region of the spectrum. Usually, the N1s region is approximated with 3 components +1 [44,46,47]. The first three components are assigned to N-C=N species (N1), corresponding to sp^2-hybridized nitrogen in the heptazine units, N-$(C)_3$ species (N2), associated with tertiary bridging nitrogen, and H-N-C species (N3), related to amino functional groups. The fourth component (N4) is attributed to π–π* shake-up transitions within the conjugated aromatic structure.

Referring again to the extensive work of V. W. Lau et al. [43], we see that they have studied in detail the possibility of fitting the N1s signal with 3 + 1 and 4 + 1 components. At the end of their work, however, they state the following: "… *increasing from three to four synthetic peaks in the fitting solution would therefore not yield additional structural insights and thus is inconsequential*". Taking this into account, we decided to opt for the series of curves from the 3 + 1 component fit (Fig. 8). The results are reported in Table 2 and residual curves are reported in Fig. S4. Although the two spectra appear very similar, slight differences are observed in the relative contributions of the fitted N1 and N2 components. Accordingly, the N2/N1 ratio obtained from the fitting procedure differs between the two samples, providing a comparative descriptor of the fitted spectral components rather than a direct quantitative measure of nitrogen-vacancy concentration.

For the sample synthesized from urea, an N_2/N_1 ratio of 0.26 was obtained, whereas the melamine-derived sample exhibits a higher value of 0.40. While this difference indicates changes in the relative

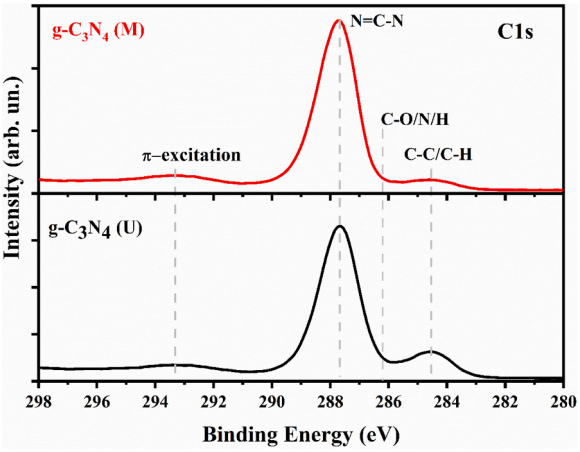

Fig. 8. XPS N1s HR spectra for samples (from top to bottom): g-C_3N_4 (M) and g-C_3N_4 (U), respectively.

contributions of the fitted nitrogen environments, it should not be interpreted as direct evidence of different nitrogen-vacancy concentrations. As discussed above, the overlap among pyridinic, tertiary, and defect-related nitrogen species, together with the intrinsic limitations of XPS peak deconvolution, prevents an unambiguous assignment of these variations to nitrogen vacancies alone. Direct identification and quantification of nitrogen vacancies would require complementary techniques specifically sensitive to these variations. Therefore, in the present work, the N_2/N_1 ratio is used only as a comparative fitting parameter describing differences in the surface nitrogen chemical environment between the two samples. Nevertheless, the XPS results clearly indicate differences in the surface chemical environment of the two samples, consistent with the different precursors employed, as evidenced by variations in both the C 1 s and N 1 s spectral regions.

XPS measurements of the valence-band region were also performed to determine the valence-band onset, expressed as the energy separation between the valence-band maximum (VBM) and the Fermi level (E_F = 0 eV), for the two g-C_3N_4 samples. The VBM was estimated by linear extrapolation of the leading edge of the valence band spectrum to the background level. As shown in Fig. S5, the VBM values were determined to be (1.71 ± 0.01) eV for g-C_3N_4 (M) and (1.63 ± 0.01) eV for g-C_3N_4 (U). The upward shift of the VBM by approximately 0.08 eV for g-C_3N_4 (M) suggests a modification of the electronic structure, which may arise from changes in the local chemical environment and/or electronic interactions within the material.

3.2. *Optical properties of the samples*

Fig. 9A presents the UV–Vis diffuse reflectance spectra of the two graphitic carbon nitride samples, g-C_3N_4 (M) and g-C_3N_4 (U). Both materials exhibit strong absorption in the UV region, which is characteristic of g-C_3N_4 semiconductors. However, significant differences in their optical properties are observed.

The g-C_3N_4 (U) sample shows an absorption edge at approximately 434 nm, consistent with the typical band gap of pristine carbon nitride. In contrast, g-C_3N_4 (M) displays a clear red shift, with absorption extending to longer wavelengths, up to approximately 610 nm. This behavior indicates enhanced visible-light absorption, which can be associated with structural modifications, increased electronic delocalization, and/or the presence of defect states within the material.

Additionally, the appearance of a broad absorption tail in the 500–610 nm range can be attributed to n–π* electronic transitions, commonly related to lone-pair electrons on nitrogen atoms and structural defects [48]. The reduced reflectance of g-C_3N_4 (M) in the visible region further suggests improved light-harvesting capability compared to g-C_3N_4 (U).

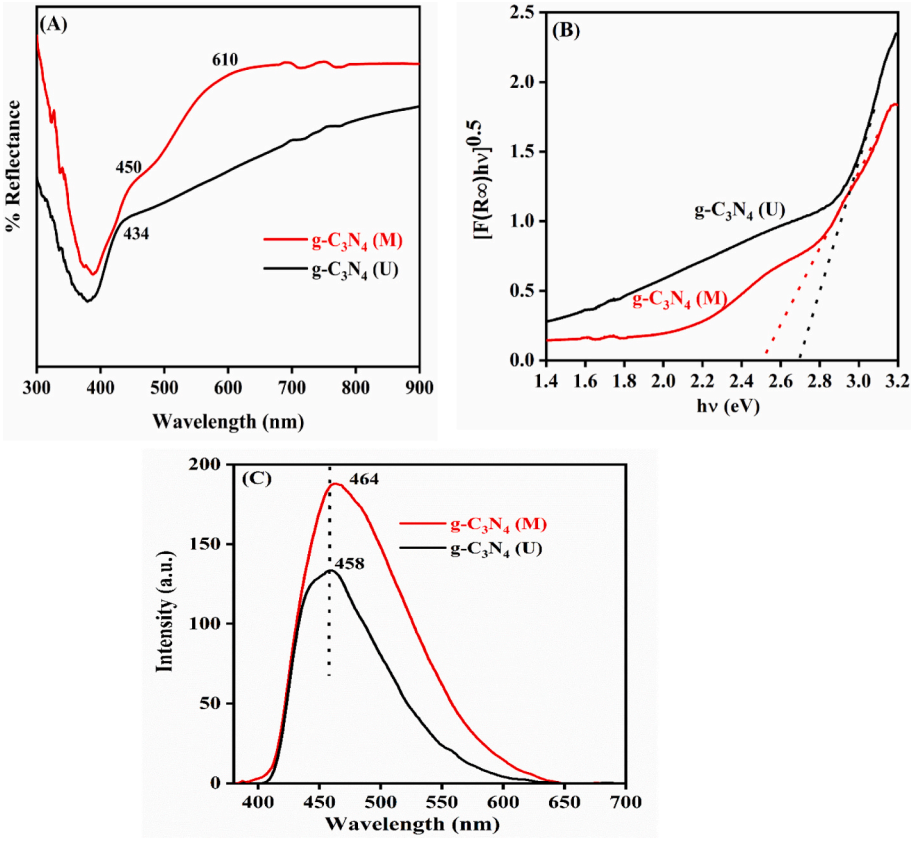

Fig. 9. (A) UV–Vis diffuse reflectance spectra (B, band gap determination and (C) PL spectra of g-C_3N_4 (U) and g-C_3N_4 (M) samples.

Such optical features are typically correlated with enhanced photocatalytic performance, as they enable more efficient utilization of the visible spectrum and can promote improved charge separation dynamics [48].

The optical band gap energies of the synthesized g-C_3N_4 samples were determined from the UV–Vis diffuse reflectance spectra using the Kubelka–Munk transformation coupled with the Tauc plot method, assuming an indirect allowed electronic transition. The band gap (E_g) was estimated by extrapolating the linear region of the $(F(R)h\nu)^{1/2}$ versus photon energy ($h\nu$) plot to the photon energy axis, where $(F(R)h\nu)^{1/2} = 0$, as presented in Fig. 9B. The corresponding Kubelka–Munk and Tauc equations used for the band gap determination are provided in the Supporting Information. The calculated band gap values are summarized in Table 1 confirm that g-C_3N_4 (M) possesses a slightly narrower band gap than g-C_3N_4 (U), supporting its extended light absorption behavior.

The PL spectra of the samples, recorded under ambient conditions (Fig. 9C), exhibit a broad emission band characteristic of graphitic carbon nitride. The emission maxima are located at 464 nm for g-C_3N_4 (M) and 458 nm for g-C_3N_4 (U), corresponding to photon energies of approximately 2.67 and 2.71 eV, respectively. These values represent the PL emission energies associated with radiative recombination and are distinct from the optical band-gap energies determined primarily from the UV–Vis diffuse-reflectance Tauc plots (2.5 eV for g-C_3N_4 (M) and 2.7 eV for g-C_3N_4 (U), Table 1). The differences between these values reflect the distinct optical processes probed by PL emission and absorption-edge analysis. The observed emission maxima are broadly consistent with the optical properties derived from UV–Vis diffuse-reflectance spectroscopy (Fig. 9A) and with previous reports on graphitic carbon nitride [49]. The observed emission is attributed to radiative recombination processes involving electronic transitions from lone-pair (LP) states in the valence band to π* antibonding states in the conduction band [50]. Compared with g-C_3N_4 (M), which exhibits a broad emission centered at 464 nm, the urea-derived g-C_3N_4 (U) displays a slight blue shift, with its emission maximum at 458 nm. This shift is consistent with its slightly higher optical band-gap energy and may reflect differences in crystallite size, structural ordering, or electronic-state distribution between the two samples [49]. Such differences in the electronic structure and radiative recombination pathways may also influence their photocatalytic behavior. However, steady-state PL spectra alone cannot establish quantitative differences in charge-carrier lifetimes or recombination kinetics; these require complementary techniques, such as time-resolved photoluminescence spectroscopy.

4. Photocatalytic activity tests

The photocatalytic degradation of chloramphenicol (CAP) and atrazine (ATZ) was investigated to evaluate the performance of the two precursor-derived g-C_3N_4 photocatalysts under UV and visible-light irradiation. Although both compounds are organic pollutants, their distinct molecular structures and physicochemical properties may lead to different adsorption behaviors and interactions with the catalyst surface.

CAP is a relatively large and flexible molecule with a nitroaromatic ring, two hydroxyl groups, and a dichloroacetamide group. These functional groups provide potential sites for hydrogen bonding and other polar interactions with the photocatalyst surface [51].

In contrast, ATZ is smaller and comparatively more hydrophobic, with a water solubility of approximately 33 mg/L. Its structure consists of an electron-deficient *s*-triazine ring bearing ethylamino and isopropylamino substituents, but no hydroxyl groups [52]. ATZ also has a higher octanol–water partition coefficient (log $K_o w \approx 2.6$) than CAP (log $K_o w \approx 1.14$), indicating a greater tendency to partition into relatively hydrophobic environments. At the working pH, both compounds are

expected to be predominantly neutral; therefore, electrostatic interactions are unlikely to be the sole factor governing their adsorption.

These molecular differences suggest that adsorption depends on the combined effects of accessible surface area, pore architecture, surface functional groups, and the chemical compatibility between the pollutant and the photocatalyst. Accordingly, the contrasting adsorption behavior of CAP and ATZ provides an opportunity to distinguish the contribution of textural properties from that of surface-chemical interactions.

4.1. Photocatalytic degradation of CAP

Photocatalytic tests were conducted to identify the photocatalyst exhibiting the highest efficiency for CAP degradation under UV and visible-light irradiation. The results are presented in Fig. 10.

As shown in Fig. 10A–C, during the 120 min dark phase, g-C_3N_4 (U) exhibited substantially higher CAP adsorption (approximately 60%) than g-C_3N_4 (M) (approximately 10%). This difference is consistent with the higher specific surface area of g-C_3N_4 (U) (41 versus 32 $m^2\ g^{-1}$) and its more developed porous tubular morphology, which may provide a greater number of accessible adsorption sites. The surface functional groups identified by FTIR may also contribute to CAP uptake through hydrogen bonding and other polar interactions involving the hydroxyl and amide groups of CAP [53,54]. Therefore, the higher CAP adsorption on g-C_3N_4 (U) is most reasonably attributed to the combined effects of surface accessibility, porous architecture, and surface chemistry, rather than to surface area alone. Nevertheless, the marked difference in dark adsorption supports a particularly important contribution from textural accessibility in the case of CAP.

Under both UV and visible light irradiation, a progressive decrease in CAP concentration was observed for both photocatalysts. After UV irradiation, CAP removal reached 25% for g-C_3N_4 (M) and 92% for g-C_3N_4 (U), while under visible light the corresponding removal efficiencies were 40% and 89%, respectively. To assess the extent of mineralization rather than merely the disappearance of the parent pollutant, TOC removal was also monitored under UV irradiation. TOC removal reached 60% for g-C_3N_4 (U) and 20% for g-C_3N_4 (M), indicating that a substantial fraction of chloramphenicol was mineralized rather than simply transformed into organic intermediate species. These results demonstrate that the superior adsorption capacity and photocatalytic activity of g-C_3N_4 (U) translate not only into higher pollutant degradation but also into more efficient mineralization.

From a structure–property–performance perspective, the superior activity of g-C_3N_4 (U) can be rationalized by considering its morphological, textural, and electronic characteristics. The tubular and porous architecture observed by SEM (Fig. 1a–b), together with its higher BET surface area (Table 2), may facilitate mass transport and increase the availability of accessible surface sites, thereby favoring CAP adsorption and subsequent surface reactions. However, the photocatalytic performance cannot be explained by adsorption alone. Despite its lower adsorption capacity, g-C_3N_4 (M) exhibits relatively improved performance under visible-light irradiation compared with its performance under UV irradiation. This behavior is consistent with its enhanced visible-light absorption, as evidenced by UV–Vis diffuse reflectance spectroscopy (DRS; Fig. 9A). The red-shifted absorption edge and narrower band gap of g-C_3N_4 (M) may enable more effective utilization of visible photons.

Furthermore, the photoluminescence (PL) results (Fig. 9C) suggest differences in the electronic structure and charge-carrier recombination behavior of the two samples. The observed emission differences may reflect precursor-dependent variations in the electronic states and recombination pathways, which can influence photocatalytic activity. XPS analysis (Fig. 8) also reveals differences in the nitrogen chemical environments, indicating that the precursor influences the surface chemistry and electronic structure of the resulting materials. These features should be considered alongside the textural properties: g-C_3N_4 (U) has a higher specific surface area, whereas g-C_3N_4 (M) exhibits a larger mesopore volume (Table 1). The larger mesopore volume of g-C_3N_4 (M) may facilitate reactant diffusion through its pore network, while the higher surface area of g-C_3N_4 (U) may increase the number of accessible adsorption sites.

The photocatalytic behavior of the two materials therefore reflects the combined effects of precursor-dependent morphology, pore architecture, surface chemistry, structural ordering, and electronic properties rather than a single structural parameter [55]. Under UV irradiation, photons provide sufficient energy for band-gap excitation, whereas under visible light, precursor-dependent differences in light absorption and electronic states may become more influential. Nitrogen-related defects have been proposed to introduce states within the band gap and modify charge-carrier dynamics; however, the specific contribution of such defects cannot be established from the present results alone [56].

4.1.1. Role of reactive oxygen species in chloramphenicol degradation

To identify the reactive species responsible for chloramphenicol (CAP) degradation over the most active photocatalyst, g-C_3N_4 (U), radical trapping experiments were carried out under UV irradiation. CAP solution (10 mg/L) was treated with three scavengers: isopropanol (IPA, 10 mmol L^{-1}) for hydroxyl radicals (·OH), p-benzoquinone (BQ, 1 mmol L^{-1}) for superoxide radicals ($\cdot O_2^-$), and ethylenediaminetetraacetic acid (EDTA, 1 mmol L^{-1}) for photogenerated holes (h^+). The corresponding results are presented in Fig. S6.

In the absence of scavengers, CAP degradation reached approximately 92%, confirming the excellent photocatalytic activity of g-C_3N_4

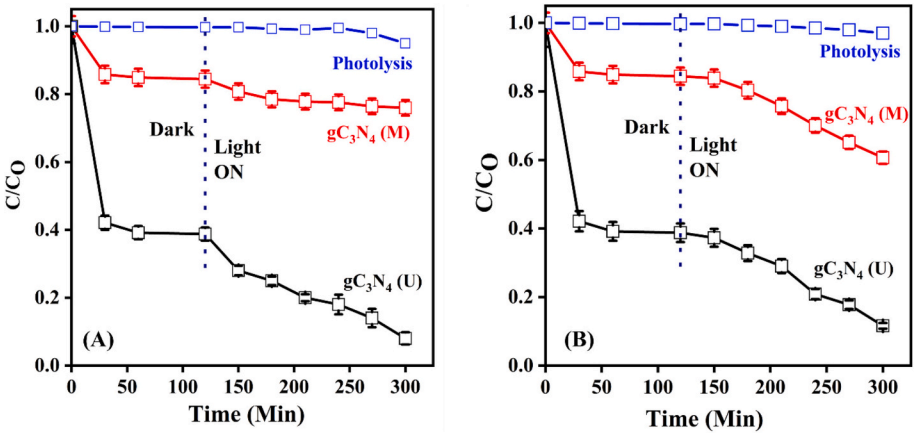

Fig. 10. Photocatalytic adsorption (120 min "dark phase") and degradation (180 min "irradiation phase") of CAP (25 ppm of CAP; 0.25 g catalyst; 50 mL solution) A) under UV light; B) under visible light.

(U). The addition of IPA caused only a slight decrease in degradation efficiency to 88%, indicating that hydroxyl radicals play only a minor role in the degradation process. In contrast, the addition of BQ dramatically reduced CAP degradation to approximately 23%, demonstrating that superoxide radicals ($\cdot O_2^-$) are the dominant reactive species. The presence of EDTA decreased the degradation efficiency to about 65%, indicating that photogenerated holes also contribute to the oxidation process, although to a lesser extent than $\cdot O_2^-$ radicals.

4.2. Photocatalytic degradation of atrazine

The photocatalytic degradation of atrazine (ATZ) under UV irradiation is shown in Fig. 11. During the dark phase, the ATZ concentration decreased by approximately 20% and 8% in the presence of g-C_3N_4 (M) and g-C_3N_4 (U), respectively, indicating a higher adsorption affinity of the melamine-derived sample toward ATZ molecules.

This behavior may be associated with precursor-dependent differences in surface chemistry and the local chemical environment of nitrogen species. In particular, XPS analysis (Fig. 8) reveals differences in the relative contributions of the fitted nitrogen components between the two photocatalysts. Previous studies, such as that reported by Peng et al. [57], have suggested that nitrogen vacancies may influence the adsorption of ATZ molecules. However, the observed differences in the fitted XPS components in the present study cannot be assigned uniquely to nitrogen vacancies. The higher atrazine adsorption observed for g-C_3N_4 (M) is therefore discussed in terms of possible differences in surface chemical environments and structural ordering, without establishing a defect-driven adsorption mechanism.

Specifically, N 1 s deconvolution results (Table 2) show a higher N_2/N_1 (tertiary-N/N–C=N) ratio for g-C_3N_4(M) (0.40) than for g-C_3N_4(U) (0.26). This ratio is considered exclusively as a comparative descriptor of the relative contributions of different surface nitrogen chemical environments and should not be interpreted as direct evidence of nitrogen vacancies or differences in their concentration. The observed variations in surface nitrogen chemistry may contribute to differences in the interactions between the photocatalyst surface and ATZ molecules, including potential interactions involving the triazine ring and secondary amine groups. Therefore, the higher ATZ adsorption observed for g-C_3N_4(M) is tentatively associated with differences in surface chemical environments rather than being directly attributed to nitrogen-vacancy-related adsorption sites. In addition, the higher degree of structural ordering and larger aromatic domains of g-C_3N_4 (M) (Table 1) may facilitate π–π interactions between the heptazine framework and the aromatic triazine ring of ATZ, an interaction expected to be less pronounced for the smaller and less ordered domains of g g-C_3N_4 (U) [58]. Consequently, ATZ adsorption appears to be governed primarily by the chemical nature of the surface active sites rather than by the total specific surface area. This surface-chemistry-dependent adsorption behavior may explain why g-C_3N_4(M) exhibits stronger ATZ adsorption in the dark despite its lower BET surface area (32 vs 41 $m^2\ g^{-1}$). This contrasts with the behavior observed for CAP, whose adsorption is mainly favored by the higher surface area and porous morphology of g-C_3N_4(U).

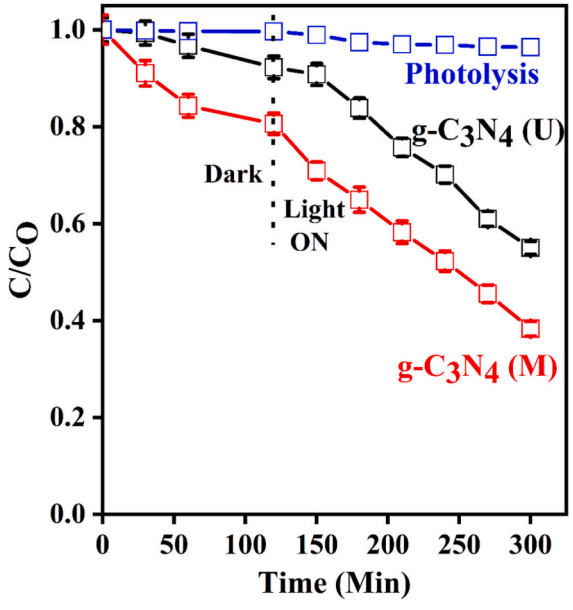

Fig. 11. Photocatalytic adsorption (120 min "dark phase") and degradation (180 min "irradiation phase") of ATZ (10 ppm of ATZ; 0.25 g catalyst; 50 mL solution) under UV light.

However, a different trend is observed under UV irradiation. Both g-C_3N_4 (M) and g-C_3N_4 (U) exhibit very similar degradation kinetics, indicating that under these conditions the influence of adsorption-related surface properties becomes less significant. Instead, the photocatalytic process is predominantly governed by direct band-gap excitation of the semiconductor. Since both samples efficiently absorb UV photons despite their differences in visible-light absorption and electronic structure, the influence of precursor-dependent morphology, surface chemistry, and defect-related electronic properties on the overall degradation efficiency becomes less pronounced. TOC removal was also monitored under UV irradiation to assess the mineralization efficiency of the photocatalytic process. TOC removal reached 40% for g-C_3N_4 (M) and 26% for g-C_3N_4 (U). Although both photocatalysts promoted only partial mineralization of atrazine, the higher TOC removal achieved by g-C_3N_4 (M) is consistent with its greater adsorption affinity toward ATZ and its more efficient photocatalytic degradation. This result further confirms that, for atrazine, surface chemistry and adsorption characteristics play a more important role than the total specific surface area in determining the overall photocatalytic performance.

4.2.1. Role of reactive oxygen species in atrazine degradation

To identify the reactive species responsible for ATZ degradation over the most active photocatalyst, g-C_3N_4 (M), radical trapping experiments were carried out under UV irradiation. Atrazine solution (10 mg/L) was treated with three scavengers: isopropanol (IPA, 10 mmol L^{-1}) for hydroxyl radicals (·OH), p-benzoquinone (BQ, 1 mmol L^{-1}) for superoxide radicals ($\cdot O_2^-$), and ethylenediaminetetraacetic acid (EDTA, 1 mmol L^{-1}) for photogenerated holes (h^+). The corresponding results are presented in Fig. S7.

In the absence of scavengers, atrazine degradation reached approximately 63%, confirming the photocatalytic activity of g-C_3N_4 (M). The addition of IPA decreased the degradation efficiency to about 43%, indicating that hydroxyl radicals play only a limited role in the degradation process. The presence of BQ reduced the degradation efficiency to approximately 37%, demonstrating the important participation of superoxide radicals. An even larger inhibition was observed in the presence of EDTA, where the degradation efficiency decreased to approximately 39%, indicating that photogenerated holes are the predominant reactive species, while superoxide radicals also make a significant contribution.

Although the estimated valence-band potentials of g-C_3N_4(M) (+1.84 V vs. NHE) is less positive than the reference potential considered for direct •OH generation (+1.99 V vs. NHE), a contribution from •OH-related pathways cannot be excluded. Interestingly, g-C_3N_4(M), which was employed for ATZ degradation, exhibits a higher XPS-derived N_2/N_1 ratio than g-C_3N_4(U) (0.40 vs. 0.26).

As discussed by Landi et al. [59], nitrogen-vacancy-related defects in g-C_3N_4 (M) may introduce localized electronic states within the band gap, potentially influencing charge trapping and interfacial electron-transfer processes. If present, such states could affect electron-mediated oxygen reduction and the formation of $\bullet O_2^-$, which may subsequently participate in reactions involving peroxide intermediates,

such as H_2O_2, and potentially lead to the formation of small amounts of •OH. This indirect pathway would not require direct oxidation of water or hydroxide ions by valence-band holes.

4.3. Photocatalytic nitrogen fixation

To evaluate the photocatalytic performance of the prepared samples, g-C_3N_4 (M) and g-C_3N_4 (U), their photocatalytic N_2 fixation activity was first investigated in the absence of sacrificial agents. The produced NH_4^+ was quantified using the Nessler method, and the corresponding calibration curve is shown in Fig. S1. Representative photographs of the calibration solutions are reported in Fig. S2. Control experiments performed in the absence of light, N_2, or photocatalyst, together with additional tests carried out in the presence of the sacrificial agents under dark conditions, showed no detectable NH_4^+ formation (Fig. S9). These results confirm that the detected NH_4^+ originates from the photocatalytic reduction of N_2 and exclude significant contributions from external contamination or side reactions involving the sacrificial agents.

As shown in Fig. 12, both samples exhibit a nearly linear increase in NH_4^+ concentration with irradiation time, indicating a steady photocatalytic process. However, a significant difference in activity is observed between the two materials. After 4 h of irradiation, g-C_3N_4 (M) achieves an ammonia production rate of approximately 27 μmol g^{-1} h^{-1}, whereas g-C_3N_4 (U) reaches only 4.7 μmol g^{-1} h^{-1}.

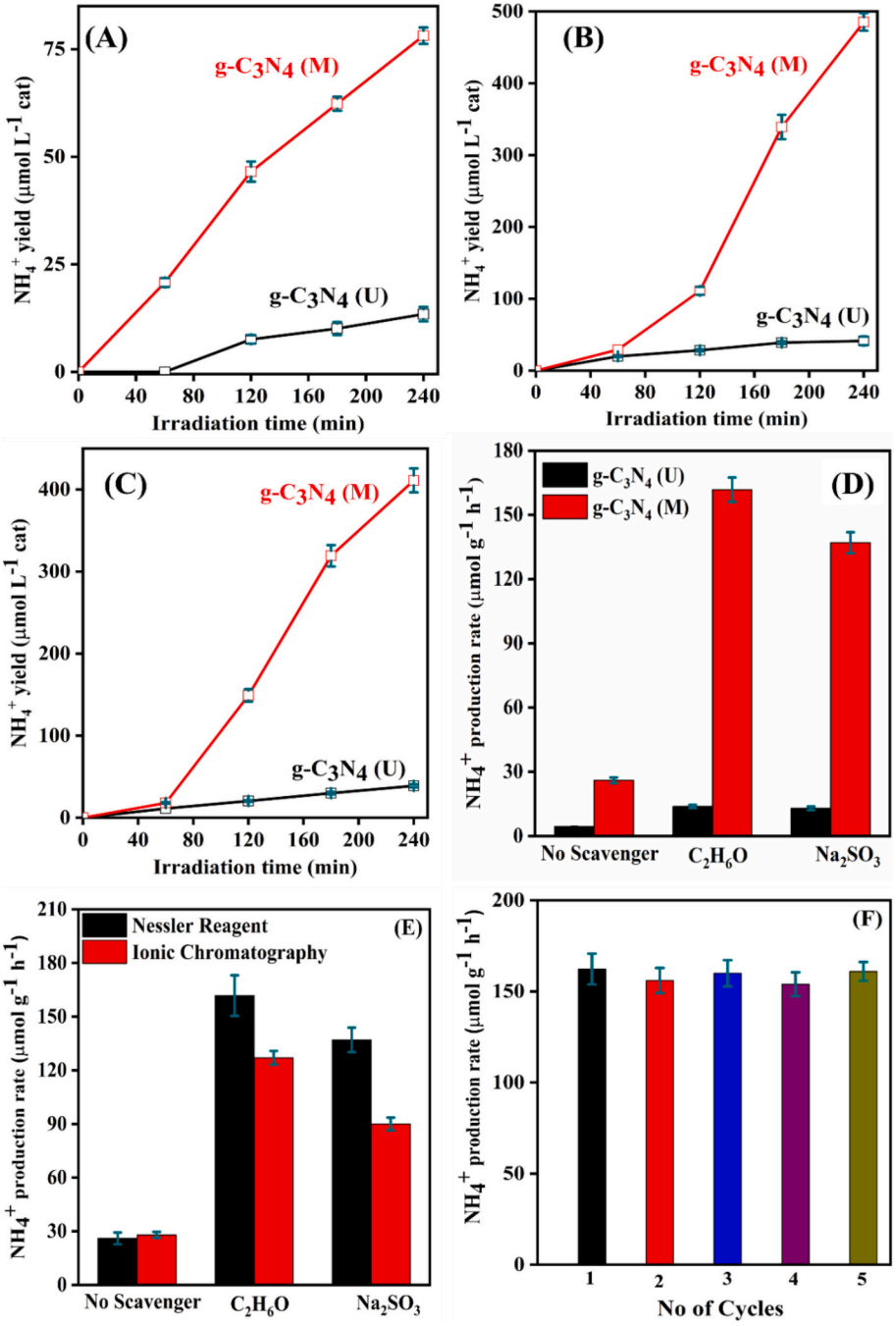

Fig. 12. Photocatalytic NH_4^+ production curves A) without scavengers; B) with 40% vol CH_3OH; C) 0.25 g/L Na_2SO_3; D) Comparison of ammonia production rates after 3 h of irradiation E) Comparison of NH_4^+ production rates determined by Nessler reagent and ion chromatography over g-C_3N_4 (M) and F) Cycling experiments with g-C_3N_4 (M) under UV irradiation.

The superior performance of g-C_3N_4(M) may be associated with its precursor-dependent structural, surface chemical, and electronic properties. XPS analysis reveals differences in the relative contributions of surface nitrogen chemical environments between the two photocatalysts, without providing direct evidence of nitrogen vacancies or their concentration. Although nitrogen-related defects have been reported to promote N_2 adsorption and activation [60], their presence and specific contribution to the photocatalytic activity observed in the present study cannot be established from the available XPS data.

Therefore, the enhanced N_2 fixation activity of g-C_3N_4(M) cannot be unambiguously attributed to nitrogen-vacancy-mediated adsorption or activation mechanisms. In addition, UV–Vis results (Fig. 9A) indicate that g-C_3N_4(M) exhibits enhanced visible-light absorption and a narrower optical band gap, potentially favoring light harvesting and photogenerated charge-carrier generation under suitable irradiation conditions. However, despite these favorable optical properties, the overall ammonia production rates remain relatively low compared with the literature values reported in Table 3. This behavior may be partly associated with charge-carrier recombination losses. Indeed, PL analysis (Fig. 9C) reveals radiative recombination processes in the investigated materials, suggesting that recombination may compete with the utilization of photogenerated charge carriers in the nitrogen reduction reaction. Consequently, charge-carrier recombination could limit the availability of electrons for N_2 reduction and contribute to the relatively low NH_4^+ production rates.

The photocatalytic activity is significantly enhanced in the presence of hole scavengers such as ethanol (EtOH) and Na_2SO_3, as shown in Fig. 12B and C. Upon light irradiation, the photocatalyst generates electron–hole pairs, with electrons in the conduction band and holes in the valence band. However, water oxidation is kinetically slow due to its high oxidation potential ($E^\circ \approx +1.23$ V vs NHE), which limits the overall efficiency of the process. In contrast, hole scavengers such as ethanol (EtOH/EtOH(ox), $E^\circ \approx +0.084$ V vs NHE) and Na_2SO_3 ($SO_3^{2-}/SO_3^{\cdot -}$, $E^\circ \approx +0.73$ V vs NHE) [73] are more readily oxidized, effectively consuming photogenerated holes.

This behavior is also consistent with the electronic structure determined by VB-XPS. The valence-band maximum (VBM) of g-C_3N_4 (M) (1.71 ± 0.01 eV) is slightly higher than that of g-C_3N_4 (U) (1.63 ± 0.01 eV), indicating a stronger oxidation capability of photogenerated holes in the melamine-derived sample. Because ethanol possesses a considerably lower oxidation potential than sulfite, hole transfer to ethanol is thermodynamically more favorable, resulting in more efficient hole scavenging and stronger suppression of electron–hole recombination. As a result, the presence of these sacrificial agents suppresses electron-hole recombination and increases the availability of electrons for the reduction of N_2 to NH_4^+. This leads to a substantial enhancement in photocatalytic nitrogen fixation performance. In particular, in the presence of CH_3OH and Na_2SO_3, the NH_4^+ production rates for g-C_3N_4 (M) increase to 162.33 and 137.13 μmol g^{-1} h^{-1}, respectively, while those for g-C_3N_4 (U) rise to 13.89 and 13.02 μmol g^{-1} h^{-1}.

To independently validate the NH_4^+ production of the best-performing photocatalyst, g-C_3N_4 (M), ammonia was also quantified by ion chromatography (IC), as shown in Fig. 12(E). IC analysis yielded NH_4^+production rates of 28, 127, and 90 μmol g^{-1} h^{-1} under water, ethanol, and Na_2SO_3 conditions, respectively, and these values are considered the primary quantitative results reported in this work. The Nessler colorimetric method showed excellent agreement with IC in the absence of scavengers (27 vs. 28 μmol g^{-1} h^{-1}), but overestimated NH_4^+ production by approximately 20–35% in the presence of ethanol and Na_2SO_3 (162.33 and 137.13 μmol g^{-1} h^{-1}, respectively). This discrepancy is attributed to the well-documented susceptibility of the Nessler reagent (K_2HgI_4) to interference from reducing species, including sulfite and ethanol oxidation byproducts, which can perturb the Hg–NH_2 colorimetric complex and lead to an overestimation of the apparent NH_4^+ concentration [74]. In contrast, ion chromatography directly separates and quantifies NH_4^+ and is not affected by these optical interferences. Therefore, IC is considered the most reliable method for evaluating the nitrogen-fixation performance of g-C_3N_4 photocatalysts in scavenger-containing reaction systems.

The markedly higher activity of g-C_3N_4 (M) is consistent with its higher density of defect sites, as indicated by XPS analysis (Fig. 8), which facilitates N_2 adsorption and activation. In addition, the more compact and ordered morphology observed by TEM analysis (Fig. 1 g-h) for g-C_3N_4 (M) may contribute to improved charge transport within the material, favoring more efficient separation and migration of photogenerated carriers.

Conversely, although g-C_3N_4 (U) exhibits a more porous and tubular structure with higher surface area, such morphology-while beneficial for adsorption-driven processes-appears less effective for reactions dominated by charge transfer, such as N_2 reduction. In this case, the higher density of structural defects and lower crystallinity may promote charge recombination, limiting the availability of electrons for the reduction reaction.

To evaluate the operational stability of the best-performing photocatalyst, g-C_3N_4 (M) was tested over five consecutive photocatalytic

Table 3
Comparison of experimental results with literature data. Where lamp power (W) and production rate are reported on a consistent molar, mass-normalized basis (μmol·g^{-1}·h^{-1}), a power-normalized rate is included to account for differences in irradiation intensity across studies.

Photocatalyst	Light source	Catalyst amount (mg)	Hole scavenger	Production rates (μmol·g^{-1}_h^{-1}.	Normalized rate (μmol g^{-1} h^{-1} W^{-1})	Reference
Goethite (α-FeO(OH))	UVC tubular lamp	50	None	20.6	–	[61]
ZnO/cu	300 W xenon lamp	20	None	68.1	0.23	[62]
$Ni_2P/Cd_{0.5}Zn_{0.5}S$	300 W Xe lamp	20	None	254	0.85	[63]
g-C_3N_4-N_3C	300 W Xe (AM-1.5)	10	10 ml methanol	1915	6.38	[64]
1.0 wt% NiS/CdS	300 W Xe	100	None	700	2.3	[65]
F-V-TiO_2	300 W Xe lamp	500	None	206	0.69	[66]
Bi_5O_7Br nanotubes	300 W Xe lamp, 400 nm cutoff	250	None	1380	4.60	[67]
Cs_2O-promoted Os–au	300 W Xe	–	None	2685	8.95	[68]
CoMoB/CN-$TH_{3/3}$	300 W Xe lamp	50	10% methanol	2164.5	7.22	[69]
Pure g-C_3N_4	300 W Xe lamp	50	5% methanol	112.06 (μmol·L^{-1}·h^{-1})	–	[70]
g-C_3N_4	250 W high-pressure sodium lamp	200	0.789 g/L ethanol	6.32 mg/L h^{-1} g_{cat}^{-1}	–	[71]
Boron-doped carbon nitride	100 mW·cm^{-2} xenon lamp	0.5 mg·ml^{-1}		0.93mmolh^{-1} g^{-1}	–	[72]
g-C_3N_4 (M)	UV lamps (32 W)	100	40% ethanol	162.33	5.07	This work

*Power-normalized activity (umol g^{-1} h^{-1} W^{-1}) is the production rate divided by the nominal electrical lamp power.

cycles using 40% ethanol under identical reaction conditions (Fig. 12F). The NH_4^+ production rate remained nearly constant, with only an approximately 5% decline in activity after the fifth cycle. This minor decrease may plausibly arise from small catalyst losses during recovery and handling or from subtle photo-induced surface changes that are not readily detectable by the characterization methods employed. These possibilities remain tentative, as their individual contributions were not independently quantified.

Post-cycle XRD analysis (Fig. S8A) showed no discernible differences from the pristine material, indicating that no detectable bulk structural degradation occurred during the cycling tests. In addition, the FTIR spectrum of the recovered catalyst (Fig. S8B) showed no new absorption bands or measurable shifts in the characteristic vibrational features. These findings provide no evidence of substantial changes in the bulk structure or detectable changes in the characteristic surface chemical groups. Overall, the results support the structural stability and recyclability of g-C_3N_4 (M) under the investigated conditions, while the precise origin of the small activity decline remains unresolved.

Notably, the obtained ammonia production rates are comparable to those reported for several metal-free or low-cost photocatalytic systems (Table 3), while being achieved under a substantially lower lamp power (32 W) than that employed in many literature studies (typically 300–500 W Xe lamps). To provide a more meaningful comparison, Table 3 also reports a power-normalized activity (μmol g^{-1} h^{-1} W^{-1}) for all studies in which both the lamp power and ammonia production rate were reported on a consistent mass-normalized basis. Although this normalization does not account for differences in reactor geometry, photon flux, spectral distribution, or irradiation efficiency, it provides a useful first-order comparison of the reported photocatalytic performances. Based on this normalization, g-C_3N_4 (M) exhibits a power-normalized activity of 5.07 μmol g^{-1} h^{-1} W^{-1}, which is higher than those reported for several representative photocatalysts, including ZnO/Cu (0.23), $Ni_2P/Cd_{0.5}Zn_{0.5}S$ (0.85), F-V-TiO_2 (0.69), and NiS/CdS (2.33), despite operating under a 32 W UV source rather than the 300 W Xe lamps commonly employed in these studies.

It should be emphasized that direct quantitative comparisons between different studies should be interpreted with caution because photocatalytic performance is also influenced by catalyst loading, reactor configuration, light spectrum, photon flux, reaction conditions, and analytical methodology. Nevertheless, the present comparison demonstrates that precursor-engineered pristine g-C_3N_4 can achieve highly competitive nitrogen-fixation performance without the need for expensive noble-metal cocatalysts or sophisticated multicomponent architectures.

4.4. Proposed photocatalytic mechanism

To gain further insight into the origin of the different photocatalytic performances of the synthesized materials, the band-edge positions were estimated from the valence-band XPS measurements. The valence-band potential (E_{VB}) was calculated according to:

$$E_{VB}(vs\ NHE) = \Phi_{analyzer} + E_{VB,onset} - 4.44 \quad (3)$$

where $\varphi_{analyzer}$ is the work function of the XPS analyzer (4.573 eV), $E_{VB,onset}$ is the energy separation between the valence-band maximum and the Fermi level, determined from the onset of the XPS valence-band spectrum, and 4.44 eV is the absolute potential of the NHE relative to the vacuum level. The conduction-band potential (E_{CB}) was subsequently obtained from:

$$E_{CB} = E_{VB} - E_g \quad (4)$$

where E_g is the optical band gap determined from the Tauc plots. Based on these calculations, the valence- and conduction-band potentials were estimated to be +1.84 V and − 0.66 V vs NHE for g-C_3N_4 (M) and + 1.76 V and − 0.94 V (vs NHE for g-C_3N_4 (U), respectively.

The estimated band alignment (Fig. 13) provides a rational explanation for the photocatalytic degradation mechanism. The conduction-band potentials of both photocatalysts are considerably more negative than the reduction potential of the $O_2/\cdot O_2^-$ couple (−0.33 V vs NHE), indicating that photogenerated electrons can readily reduce dissolved oxygen to superoxide radicals. In contrast, the valence-band potentials are slightly less positive than the oxidation potential of the $OH^-/\cdot OH$ couple (+1.99 V vs NHE), suggesting that the direct generation of hydroxyl radicals is thermodynamically less favorable. This interpretation is fully consistent with the radical trapping experiments performed on the most active photocatalysts for each pollutant, namely g-C_3N_4 (U) for CAP (Fig. S6) and g-C_3N_4 (M) for ATZ (Fig. S7). In both systems, the addition of p-Q produced the most pronounced suppression of photocatalytic activity, demonstrating that $\cdot O_2^-$ is the dominant reactive oxygen species responsible for pollutant degradation. Conversely, the comparatively small decrease observed after IPA addition confirms that hydroxyl radicals play only a minor role in the overall process. Although the estimated valence-band potentials are slightly less positive than the $OH^-/\bullet OH$ oxidation potential, the difference is relatively small (0.15–0.23 V), and therefore a limited formation of hydroxyl radicals through surface-mediated oxidation pathways or localized electronic states associated with surface defects cannot be completely excluded. The significant inhibition observed in the presence of EDTA clearly demonstrates that photogenerated holes also participate directly in pollutant oxidation.

In the case of nitrogen fixation, both photocatalysts possess conduction-band potentials substantially more negative than the reduction potential of the N_2/NH_4^+ couple (−0.092 V vs NHE) (Fig.S10), indicating that the reduction of molecular nitrogen is thermodynamically feasible on both materials. Nevertheless, g-C_3N_4 (M) exhibits a markedly higher NH_4^+ production rate despite its less negative conduction-band potential. This result clearly demonstrates that the nitrogen-fixation activity is not governed solely by the thermodynamic reduction potential but rather by the combined influence of structural ordering, electronic structure, defect-related surface chemistry, and charge-carrier dynamics. The higher crystallinity and more condensed polymeric framework of g-C_3N_4 (M) may contribute to more efficient charge transport, while precursor-dependent surface chemistry may influence N_2 adsorption and activation. Literature reports suggest that nitrogen-related defects may facilitate N_2 adsorption and activation [75–77]; however, the existence and concentration of nitrogen vacancies cannot be confirmed solely from our XPS data. Therefore, the possible contribution of defect-related sites remains a hypothesis rather than an established mechanism in the present study. Overall, the higher nitrogen-fixation activity of g-C_3N_4 (M) is best interpreted in terms of the combined structural, electronic, and surface properties of the material, without attributing its superior performance specifically to nitrogen-vacancy-mediated activation.

The role of sacrificial agents can also be rationalized by considering the thermodynamic driving force for hole oxidation, defined as:

$$\Delta E = E_{VB} - E_{redox} \quad (5)$$

where E_{redox} is the oxidation potential of the sacrificial agent. Using oxidation potentials of +0.084 V vs NHE for ethanol and + 0.73 V vs NHE for sulfite, the corresponding driving forces for g-C_3N_4 (M) are calculated to be 1.76 V and 1.11 V, respectively, whereas those for g-C_3N_4 (U) are 1.68 V and 1.03 V, respectively. The larger thermodynamic driving force associated with ethanol oxidation explains its more efficient hole-scavenging ability and the consequent suppression of electron–hole recombination.

These thermodynamic and kinetic considerations are in agreement with the experimental results, where ethanol consistently produced higher NH_4^+ evolution rates than Na_2SO_3 for both photocatalysts.

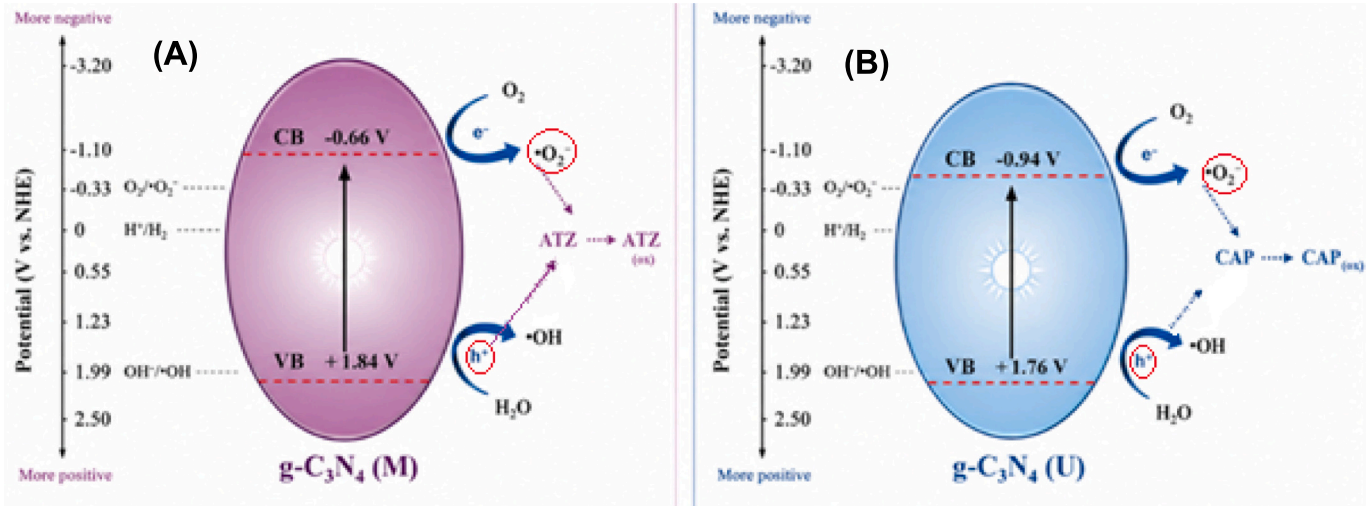

Fig. 13. Proposed photocatalytic degradation mechanisms for (A) atrazine using g-C_3N_4 (M) and (B) chloramphenicol (CAP) using g-C_3N_4 (U). Superoxide radicals ($•O_2^-$) are identified as the dominant reactive oxygen species, while hydroxyl radicals (•OH) represent only a minor secondary reactive species and are not the primary oxidant under the investigated conditions.

5. Conclusions

This work presents a systematic comparison of graphitic carbon nitride (g-C3N4) synthesized from urea and melamine, providing a comprehensive understanding of how precursor selection influences structure-property-performance relationships in photocatalytic pollutant degradation and nitrogen fixation. The results demonstrate that precursor choice strongly influences morphology, crystallinity, surface chemistry, and electronic structure, contributing to the observed differences in photocatalytic performance across the investigated reactions.

The urea-derived g-C3N4 exhibits a hollow and porous morphology with higher specific surface area, as confirmed by SEM and BET analyses, which favors pollutant adsorption and surface accessibility. FTIR and XPS results further indicate differences in surface functional groups and chemical environments that may contribute to interactions with pollutant molecules. As a consequence, this material shows superior performance in chloramphenicol removal, where adsorption plays a significant role.

In contrast, the melamine-derived g-C3N4 displays a more compact and crystalline structure, as evidenced by XRD and TEM, along with enhanced visible-light absorption and a narrower band gap revealed by UV–Vis spectroscopy. PL analysis provides information on radiative charge-carrier recombination, while XPS reveals differences in the relative contributions of surface nitrogen chemical environments without directly establishing the presence or concentration of nitrogen vacancies. These combined structural, surface chemical, and optical characteristics may contribute to the different photocatalytic behavior observed for the melamine-derived material.

Photocatalytic tests clearly highlight a reaction-dependent behavior. The urea-derived sample performs significantly better in chloramphenicol removal, reaching up to ~60% CAP removal during the dark phase and ~ 92% under UV irradiation, compared to only ~10% and ~ 25% for the melamine-derived sample. This enhanced performance is consistent with its higher surface area and porous tubular morphology (SEM, BET), which promote pollutant adsorption and surface interactions. In addition, FTIR results suggest the presence of surface functional groups that may facilitate hydrogen bonding with chloramphenicol molecules, further enhancing its adsorption capacity.

In contrast, for atrazine degradation under UV irradiation, both materials exhibit comparable activity despite their structural differences, although their adsorption behavior differs (~20% for g-C3N4(M) vs ~8% for g-C3N4(U)). This suggests that, under the investigated UV irradiation conditions, differences in surface properties have a less pronounced influence on the overall degradation behavior than in the case of CAP. Both materials can undergo band-gap excitation under UV irradiation, which may contribute to their comparable photocatalytic performance. In contrast, the melamine-derived g-C3N4 exhibits superior performance in photocatalytic nitrogen fixation, reaching an ammonia production rate of approximately 127 μmol g^{-1} h^{-1} as determined by ion chromatography, or 162.33 μmol g^{-1} h^{-1} according to the Nessler method, in the presence of ethanol as a hole scavenger. This behavior may be associated with the combined influence of structural ordering, optical properties, surface chemical environments, and charge-carrier processes, rather than being directly attributed to nitrogen-related defect sites.

Overall, this study demonstrates that precursor selection is a simple yet effective approach for tuning the photocatalytic behavior of g-C_3N_4. Furthermore, the results reveal an application-dependent trade-off between the two precursor-derived g-C_3N_4 photocatalysts. Neither material is universally superior; rather, their relative performance depends on the physicochemical processes involved in the target reaction. The urea-derived g-C3N4 is better suited for chloramphenicol degradation, in which adsorption and surface accessibility play important roles, whereas the melamine-derived material exhibits better performance under the investigated photocatalytic nitrogen fixation conditions. These findings highlight precursor selection as a rational strategy for tailoring g-C3N4 to specific environmental photocatalytic applications rather than maximizing a single performance metric.

This application-dependent behavior can be rationalized by considering the different material properties involved in each photocatalytic process. Pollutant removal may be strongly influenced by morphology, surface area, and surface chemistry, whereas photocatalytic nitrogen fixation also depends on the electronic properties of the material and the availability of photogenerated charge carriers. By systematically correlating comprehensive physicochemical characterization with photocatalytic performance, this work provides an integrated structure–property–performance perspective that helps rationalize the divergent behavior of precursor-derived g-C_3N_4 and offers useful considerations for the design of carbon nitride photocatalysts for specific environmental remediation and sustainable energy applications.

Despite these promising results, several limitations should be acknowledged. First, experiments were primarily conducted under 365 nm UV irradiation, while visible-light data were available only for CAP; therefore, performance under natural solar irradiation remains to be investigated. Second, the highest ammonia production rate was

obtained in the presence of ethanol as a sacrificial hole scavenger, a condition that limits direct practical applicability. The scavenger-free rate of approximately 28 μmol g^{-1} h^{-1}, determined by ion chromatography, provides a more realistic benchmark. Third, pollutant degradation and nitrogen fixation were investigated separately, and their simultaneous operation in a single reactor remains unexplored. Fourth, degradation intermediates were not identified, and TOC removal remained incomplete (60% and 20% for CAP; 26% and 40% for ATZ, respectively, for the two materials). Therefore, LC-MS analysis and ecotoxicity assays are needed to identify transformation products and assess the environmental safety of treated effluents. Furthermore, experiments were performed in ultrapure water at a single pollutant concentration under batch conditions, leaving the effects of real water matrices, catalyst recovery, and scalability unaddressed. Finally, ammonia quantification may depend on the analytical method; therefore, ion chromatography (IC) values are reported as the primary results, with differences from Nessler-based measurements considered when interpreting the results. In addition, the identification and quantification of nitrogen vacancies would require complementary characterization techniques, such as electron paramagnetic resonance (EPR) spectroscopy, which was not performed in this study.

Future research should focus on solar-driven photocatalysis, scavenger-free nitrogen fixation, and the simultaneous degradation of pollutants and ammonia production in integrated systems. LC-MS analysis, ecotoxicity assessment, and further TOC measurements are also essential to evaluate degradation pathways, mineralization, and environmental safety. Additionally, testing real wastewater and natural water matrices, investigating catalyst recovery and reuse, and applying strategies such as doping, defect engineering, co-catalyst loading, and heterojunction construction could improve photocatalytic efficiency and support the practical application of g-C_3N_4-based materials.

CRediT authorship contribution statement

Mohit Pathak: Writing – original draft, Methodology, Investigation, Data curation. **Vincenzo Vaiano:** Writing – review & editing, Supervision, Data curation. **Vincenzo Venditto:** Writing – review & editing, Supervision, Funding acquisition. **Serena Esposito:** Investigation, Formal analysis. **Micaela Castellino:** Investigation, Data curation. **Christophe Daniel:** Writing – review & editing, Supervision, Funding acquisition. **Olga Sacco:** Writing – review & editing, Supervision, Methodology, Investigation, Formal analysis, Conceptualization.

Declaration of generative AI and AI-assisted Technologies in the Writing Process

During the preparation of this manuscript, the authors used ChatGPT (OpenAI) to assist with English language editing, including improvements in grammar, clarity, and readability, and to provide support in the preparation and graphical organization of Fig. S10 in the Supplementary Information. The scientific content, underlying data, calculations, and interpretation of the figure were provided and verified by the authors. Following the use of this tool, the authors reviewed and edited the content as needed and take full responsibility for the accuracy, originality, and integrity of the published work.

Declaration of competing interest

The authors declare that they have no known competing financial interests or personal relationships that could have appeared to influence the work reported in this paper.

Appendix A. Supplementary data

Supplementary data to this article can be found online at https://doi.org/10.1016/j.jphotochem.2026.117819.

Data availability

Data will be made available on request.

References

[1] O. Ejiohuo, H. Onyeaka, A. Akinsemolu, O.F. Nwabor, K.F. Siyanbola, P. Tamasiga, Z.T. Al-Sharify, Ensuring water purity: mitigating environmental risks and safeguarding human health, Water Biol. Secur. 4 (2025) 100341, https://doi.org/10.1016/j.watbs.2024.100341.

[2] P.H. Gleick, Water in crisis: paths to sustainable water use, Ecol. Appl. 8 (1998) 571–579, https://doi.org/10.1890/1051-0761(1998)008%5B0571:WICPTS%5D2.0.CO;2.

[3] A. Nasibova, Generation of nanoparticles in biological systems and their application prospects, Adv. Biol. Earth Sci. 8 (2023) 140–146.

[4] Md.M. Islam, A.R. Aidid, J.N. Mohshin, H. Mondal, S. Ganguli, A.K. Chakraborty, A critical review on textile dye-containing wastewater: ecotoxicity, health risks, and remediation strategies for environmental safety, Clean. Chem. Eng. 11 (2025) 100165, https://doi.org/10.1016/j.clce.2025.100165.

[5] C. Simarro-Gimeno, E. Pitarch, F. Albarrán, A. Rico, F. Hernández, Ten years of monitoring pharmaceuticals and pesticides in the aquatic environment nearby a solid-waste treatment plant: historical data, trends and risk assessment, Environ. Pollut. 366 (2025) 125496, https://doi.org/10.1016/j.envpol.2024.125496.

[6] S. Chandra, K.B. Walsh, Microplastics in water: occurrence, fate and removal, J. Contam. Hydrol. 264 (2024) 104360, https://doi.org/10.1016/j.jconhyd.2024.104360.

[7] B. Pratap, S. Kumar, S. Nand, I. Azad, R.N. Bharagava, L.F. Romanholo Ferreira, V. Dutta, Wastewater generation and treatment by various eco-friendly technologies: possible health hazards and further reuse for environmental safety, Chemosphere 313 (2023) 137547, https://doi.org/10.1016/j.chemosphere.2022.137547.

[8] P. Döll, S. Siebert, Global modeling of irrigation water requirements, Water Resour. Res. 38 (2002) 8-1–8–10, https://doi.org/10.1029/2001WR000355.

[9] B.J. Heyde, M. Braun, L. Soufi, K. Lüneberg, S. Gallego, W. Amelung, K. Axtmann, G. Bierbaum, S.P. Glaeser, E. Grohmann, R. Arredondo-Hernández, I. Mulder, D. Pulami, K. Smalla, C. Zarfl, C. Siebe, J. Siemens, Transition from irrigation with untreated wastewater to treated wastewater and associated benefits and risks, NPJ Clean Water 8 (2025) 6, https://doi.org/10.1038/s41545-025-00438-6.

[10] X. Fang, Y. Yang, Z. Zhao, Y. Zhou, Y. Liao, Z. Guan, S. Chen, W. Fang, F. Chen, S. Zhao, Optimum nitrogen, phosphorous, and potassium fertilizer application increased Chrysanthemum growth and quality by reinforcing the soil microbial community and nutrient cycling function, Plants 12 (2023), https://doi.org/10.3390/plants12234062.

[11] G.Z.S. Ling, S.-F. Ng, W.-J. Ong, Tailor-engineered 2D cocatalysts: harnessing electron–hole redox center of 2D g-C3N4 photocatalysts toward solar-to-chemical conversion and environmental purification, Adv. Funct. Mater. 32 (2022) 2111875, https://doi.org/10.1002/adfm.202111875.

[12] S. Ali, S.U.H. Bakhtiar, A. Ismail, P.M. Ismail, S. Hayat, A. Zada, X. Wu, A. N. Alodhayb, M. Zahid, F. Raziq, J. Yi, L. Qiao, Transition metal sulfides: from design strategies to environmental and energy-related applications, Coord. Chem. Rev. 523 (2025) 216237, https://doi.org/10.1016/j.ccr.2024.216237.

[13] S. Ganesan, T. Kokulnathan, S. Sumathi, A. Palaniappan, Efficient photocatalytic degradation of textile dye pollutants using thermally exfoliated graphitic carbon nitride (TE–g–C3N4), Sci. Rep. 14 (2024) 2284, https://doi.org/10.1038/s41598-024-52688-y.

[14] G. Zhuang, J. Yan, Y. Wen, Z. Zhuang, Y. Yu, Two-dimensional transition metal oxides and chalcogenides for advanced photocatalysis: progress, challenges, and opportunities, Solar RRL 5 (2021) 2000403, https://doi.org/10.1002/solr.202000403.

[15] M. Cheng, C. Xiao, Y. Xie, Photocatalytic nitrogen fixation: the role of defects in photocatalysts, J. Mater. Chem. A 7 (2019) 19616–19633, https://doi.org/10.1039/C9TA06435D.

[16] D. Bhanderi, P. Lakhani, C.K. Modi, Graphitic carbon nitride (g-C_3N_4) as an emerging photocatalyst for sustainable environmental applications: a comprehensive review, RSC Sustain. 2 (2024) 265–287, https://doi.org/10.1039/D3SU00382E.

[17] W.-J. Ong, L.-L. Tan, Y.H. Ng, S.-T. Yong, S.-P. Chai, Graphitic carbon nitride (g-C3N4)-based photocatalysts for artificial photosynthesis and environmental remediation: are we a step closer to achieving sustainability? Chem. Rev. (2016) https://doi.org/10.1021/acs.chemrev.6b00075.

[18] A. Verma, G. Sharma, T. Wang, A. Kumar, P. Dhiman, A. García-Peñas, Graphitic carbon nitride (g-C_3N_4)-based magnetic photocatalysts for removal of antibiotics, Carbon Lett. 35 (2025) 45–73, https://doi.org/10.1007/s42823-024-00811-4.

[19] R.-H. Gao, Q. Ge, N. Jiang, H. Cong, M. Liu, Y.-Q. Zhang, Graphitic carbon nitride (g-C3N4)-based photocatalytic materials for hydrogen evolution, Front. Chem. 10 (2022), https://doi.org/10.3389/fchem.2022.1048504.

[20] G. Liao, Y. Gong, L. Zhang, H. Gao, G.-J. Yang, B. Fang, Semiconductor polymeric graphitic carbon nitride photocatalysts: the "holy grail" for the photocatalytic hydrogen evolution reaction under visible light, Energ. Environ. Sci. 12 (2019) 2080–2147, https://doi.org/10.1039/C9EE00717B.

[21] M. Aggarwal, S. Basu, N.P. Shetti, M.N. Nadagouda, E.E. Kwon, Y.-K. Park, T. M. Aminabhavi, Photocatalytic carbon dioxide reduction: exploring the role of ultrathin 2D graphitic carbon nitride (g-C3N4), Chem. Eng. J. 425 (2021) 131402, https://doi.org/10.1016/j.cej.2021.131402.

[22] Q. Xu, Z. Xia, J. Zhang, Z. Wei, Q. Guo, H. Jin, H. Tang, S. Li, X. Pan, Z. Su, S. Wang, Recent advances in solar-driven CO_2 reduction over g-C3N4-based photocatalysts, Carbon Energy 5 (2023) e205, https://doi.org/10.1002/cey2.205.
[23] L. Zhang, S. Hou, T. Wang, S. Liu, X. Gao, C. Wang, G. Wang, Recent advances in application of graphitic carbon nitride-based catalysts for photocatalytic nitrogen fixation, Small 18 (2022) 2202252, https://doi.org/10.1002/smll.202202252.
[24] P. Praus, Photocatalytic nitrogen fixation using graphitic carbon nitride: a review, ChemistrySelect 8 (2023) e202204511, https://doi.org/10.1002/slct.202204511.
[25] Y. Zheng, J. Liu, J. Liang, M. Jaroniec, S. Zhang Qiao, Graphitic carbon nitride materials: controllable synthesis and applications in fuel cells and photocatalysis, Energ. Environ. Sci. 5 (2012) 6717–6731, https://doi.org/10.1039/C2EE03479D.
[26] S. Ye, R. Wang, M.-Z. Wu, Y.-P. Yuan, A review on g-C3N4 for photocatalytic water splitting and CO_2 reduction, Appl. Surf. Sci. 358 (2015) 15–27, https://doi.org/10.1016/j.apsusc.2015.08.173.
[27] W. Lu, L. Qi, D. Dong, X. Shen, L. Xu, Y. Zhang, X. Mei, W. Qiao, X. Guo, Y. Pan, A comparison study of photocatalytic performance of g-C_3N_4 prepared from different precursors for the activation of different peroxides, Sep. Purif. Technol. 327 (2023) 124904, https://doi.org/10.1016/j.seppur.2023.124904.
[28] D. Briševac, I. Gabelica, F. Radovanović-Perić, K.T. Čop, G. Matijašić, D. Ljubas, L. Ćurković, Influence of different precursors on properties and photocatalytic activity of g-C_3N_4 synthesized via thermal polymerization, Materials 18 (2025), https://doi.org/10.3390/ma18112522.
[29] P. Negro, F. Cesano, A. Damin, R. Brescia, D. Scarano, Porous g-C3N4-based nanoarchitectures by playing with sustainable precursors: role of urea/melamine ratio on the structure/properties relationship, J. Alloys Compd. 1002 (2024) 175053, https://doi.org/10.1016/j.jallcom.2024.175053.
[30] B. Parga, M.A. Ruiz-Gómez, V. Rodríguez-González, A. Vázquez, S. Obregón, Nitrogen-rich g-C3N4 synthesized by simultaneous melamine/urea polycondensation for photocatalytic removal of tetracycline hydrochloride, Mater. Today Commun. 49 (2025) 114258, https://doi.org/10.1016/j.mtcomm.2025.114258.
[31] Z. Li, G. Gu, S. Hu, X. Zou, G. Wu, Promotion of activation ability of N vacancies to N2 molecules on sulfur-doped graphitic carbon nitride with outstanding photocatalytic nitrogen fixation ability, Chin. J. Catal. 40 (2019) 1178–1186, https://doi.org/10.1016/S1872-2067(19)63364-4.
[32] N. Iqbal, A. Afzal, I. Khan, M.S. Khan, A. Qurashi, Molybdenum impregnated g-C_3N_4 nanotubes as potentially active photocatalyst for renewable energy applications, Sci. Rep. 11 (2021) 16886, https://doi.org/10.1038/s41598-021-96490-6.
[33] J. Lu, Z. Li, B. Wu, Z. Jiang, C. Pei, Nanosheet-stacked g-C_3N_4 tubes with carbon vacancies for enhanced photocatalytic H2 evolution, ACS Appl. Nano Mater. 8 (2025) 6133–6143, https://doi.org/10.1021/acsanm.5c00363.
[34] Y. Zheng, Z. Zhang, C. Li, A comparison of graphitic carbon nitrides synthesized from different precursors through pyrolysis, J. Photochem. Photobiol. Chem. 332 (2017) 32–44, https://doi.org/10.1016/j.jphotochem.2016.08.005.
[35] J. Liu, T. Zhang, Z. Wang, G. Dawson, W. Chen, Simple pyrolysis of urea into graphitic carbon nitride with recyclable adsorption and photocatalytic activity, J. Mater. Chem. 21 (2011) 14398–14401, https://doi.org/10.1039/C1JM12620B.
[36] Y. Zhang, J. Liu, G. Wu, W. Chen, Porous graphitic carbon nitride synthesized via direct polymerization of urea for efficient sunlight-driven photocatalytic hydrogen production, Nanoscale 4 (2012) 5300–5303, https://doi.org/10.1039/C2NR30948C.
[37] Y. Miyake, G. Seo, K. Matsuhashi, N. Takada, K. Kanai, Synthesis of carbon nitride oligomer as a precursor of melon with improved fluorescence quantum yield, Mater. Adv. 2 (2021) 6083–6093, https://doi.org/10.1039/D1MA00579K.
[38] B.V. Lotsch, M. Döblinger, J. Sehnert, L. Seyfarth, J. Senker, O. Oeckler, W. Schnick, Unmasking melon by a complementary approach employing electron diffraction, solid-state NMR spectroscopy, and theoretical calculations—structural characterization of a carbon nitride polymer, Chem. Eur. J. 13 (2007) 4969–4980, https://doi.org/10.1002/chem.200601759.
[39] S. Kundoo, A.N. Banerjee, P. Saha, K.K. Chattopadhyay, Synthesis of crystalline carbon nitride thin films by electrolysis of methanol–urea solution, Mater. Lett. 57 (2003) 2193–2197, https://doi.org/10.1016/S0167-577X(02)01172-2.
[40] X. Li, J. Zhang, L. Shen, Y. Ma, W. Lei, Q. Cui, G. Zou, Preparation and characterization of graphitic carbon nitride through pyrolysis of melamine, Appl. Phys. A Mater. Sci. Process. 94 (2009) 387–392, https://doi.org/10.1007/s00339-008-4816-4.
[41] Z. Jiang, K. Qian, C. Zhu, H. Sun, W. Wan, J. Xie, H. Li, P.K. Wong, S. Yuan, Carbon nitride coupled with CdS-TiO_2 nanodots as 2D/0D ternary composite with enhanced photocatalytic H_2 evolution: a novel efficient three-level electron transfer process, Appl. Catal. Environ. 210 (2017) 194–204, https://doi.org/10.1016/j.apcatb.2017.03.069.
[42] L. Kong, J. Wang, X. Mu, R. Li, X. Li, X. Fan, P. Song, F. Ma, M. Sun, Porous size dependent g-C_3N_4 for efficient photocatalysts: regulation synthesizes and physical mechanism, Mater. Today Energy 13 (2019) 11–21, https://doi.org/10.1016/j.mtener.2019.04.011.
[43] V.W. Lau, C.-F. Lu, N. Putri Wijaya, M. Lutan, Can X-ray photoelectron spectroscopy characterize Photocatalytically relevant defects in graphitic carbon nitride? Re-examining peak assignment and quantification using model compounds, Chem. Mater. 36 (2024) 9762–9774, https://doi.org/10.1021/acs.chemmater.4c01902.
[44] L. He, M. Fei, J. Chen, Y. Tian, Y. Jiang, Y. Huang, K. Xu, J. Hu, Z. Zhao, Q. Zhang, H. Ni, L. Chen, Graphitic C_3N_4 quantum dots for next-generation QLED displays, Mater. Today 22 (2019) 76–84, https://doi.org/10.1016/j.mattod.2018.06.008.
[45] A.V. Shchukarev, D.V. Korolkov, XPS study of group IA carbonates, Cent. Eur. J. Chem. 2 (2004) 347–362, https://doi.org/10.2478/BF02475578.
[46] L. Xueyan, W. Guanlong, L. Chenrui, D. Xiaoli, Z. Xiufang, New insight into enhanced photocatalytic selectivity of g-C_3N_4 by nitrogen vacancy introduction: experimental study and theoretical calculation, Environ. Res. 212 (2022) 113390, https://doi.org/10.1016/j.envres.2022.113390.
[47] Y. Li, M. Ti, D. Zhao, Y. Zhang, L. Wu, Y. He, Facile synthesis of nitrogen-vacancy pothole-rich few-layer g-C_3N_4 for photocatalytic nitrogen fixation into nitrate and ammonia, J. Alloys Compd. 870 (2021) 159298, https://doi.org/10.1016/j.jallcom.2021.159298.
[48] L. Zhang, X. Zhou, S. Liu, H. Liu, S. Zhu, Y. Mao, Q. Yang, S. Zhu, C. Zhang, T. Wang, C. Wang, Two birds, one stone: rational design of bi-MOF/g-C_3N_4 photocatalyst for effective nitrogen fixation and pollutants degradation, J. Clean. Prod. 425 (2023) 138912, https://doi.org/10.1016/j.jclepro.2023.138912.
[49] D. Zhang, G. Tan, M. Wang, B. Li, M. Dang, H. Ren, A. Xia, The modulation of g-C3N4 energy band structure by excitons capture and dissociation, Mater. Res. Bull. 122 (2020) 110685, https://doi.org/10.1016/j.materresbull.2019.110685.
[50] E.B. Chubenko, A.V. Baglov, M.S. Leonenya, G.P. Yablonskii, V.E. Borisenko, Structure of photoluminescence spectra of oxygen-doped graphitic carbon nitride, J. Appl. Spectrosc. 87 (2020) 9–14, https://doi.org/10.1007/s10812-020-00954-y.
[51] Crystal structure of racemic chloramphenicol, Acta Crystallogr. Sect. E Crystallogr. Commun. 82 (2026) 1091–1094, https://doi.org/10.1107/S2056989026008765.
[52] Y.L. Salomón, J. Georgin, D.G.P. Allasia, M.S. Netto, C.O. Aniagor, J.O. Ighalo, D.S. P. Franco, A comprehensive review on atrazine adsorption: from environmental contamination to efficient removal technologies, Sustainability 17 (2025) 10455, https://doi.org/10.3390/su172310455.
[53] A. Mancuso, A. Pipolo, P. Iannece, L. Albarano, M. Carotenuto, G. Lofrano, G. Libralato, V. Venditto, O. Sacco, V. Vaiano, Engineered g-C_3N_4/N-TiO_2 heterostructure for enhanced visible-light photocatalytic degradation of chloramphenicol: mechanistic insight and ecotoxicological assessment of the treated effluent, J. Environ. Chem. Eng. 13 (2025) 119711, https://doi.org/10.1016/j.jece.2025.119711.
[54] L.M. Nguyen, N.T.T. Nguyen, T.T.T. Nguyen, T.T. Nguyen, D.T.C. Nguyen, T. V. Tran, Occurrence, toxicity and adsorptive removal of the chloramphenicol antibiotic in water: a review, Environ. Chem. Lett. 20 (2022) 1929–1963, https://doi.org/10.1007/s10311-022-01416-x.
[55] G. Wang, Y. Zhao, H. Ma, C. Zhang, X. Dong, X. Zhang, Enhanced peroxymonosulfate activation on dual active sites of N vacancy modified g-C_3N_4 under visible-light assistance and its selective removal of organic pollutants, Sci. Total Environ. 756 (2021) 144139, https://doi.org/10.1016/j.scitotenv.2020.144139.
[56] Z. Wang, Y. Huang, M. Chen, X. Shi, Y. Zhang, J. Cao, W. Ho, S.C. Lee, Roles of N-vacancies over porous g-C3N4 microtubes during photocatalytic NO_x removal, ACS Appl. Mater. Interfaces 11 (2019) 10651–10662, https://doi.org/10.1021/acsami.8b21987.
[57] Q. Peng, L. Ye, N. Wen, H. Chen, Y. Zhu, H. Niu, H. Tian, D. Huang, Y. Huang, Nitrogen vacancy-modified g-C_3N_4 nanosheets controlled by deep eutectic solvents for highly efficient photocatalytic atrazine degradation: non-radical dominated holes oxidation, Sep. Purif. Technol. 354 (2025) 128879, https://doi.org/10.1016/j.seppur.2024.128879.
[58] F. Xiao, J.J. Pignatello, Interactions of triazine herbicides with biochar: steric and electronic effects, Water Res. 80 (2015) 179–188, https://doi.org/10.1016/j.watres.2015.04.040.
[59] A. Landi, F. Ambrosio, N. Bianchi, M. Loriso, L. Malavasi, A. Profumo, J. Wiktor, A. Peluso, Nitrogen vacancies in graphitic carbon nitride and their role in heterogeneous photocatalysis, Mater. Horiz. 13 (2026) 6657–6664, https://doi.org/10.1039/d6mh00462h.
[60] R. Huang, X. Li, W. Gao, X. Zhang, S. Liang, M. Luo, Recent advances in photocatalytic nitrogen fixation: from active sites to ammonia quantification methods, RSC Adv. 11 (2021) 14844–14861, https://doi.org/10.1039/D0RA10439F.
[61] C.A. Podence Alves, P.H. Palharim, B. Pratto, A.L. da Silva, D. Gouvêa, B. Ramos, Photocatalytic ammonia synthesis from nitrogen in water using iron oxides: comparative efficiency of goethite, magnetite, and hematite, J. Photochem. Photobiol. A Chem. 460 (2025) 116159, https://doi.org/10.1016/j.jphotochem.2024.116159.
[62] R. Yang, J. Liu, X. Sun, C. Wang, B. Jiang, Enhancing photocatalytic N2 fixation efficiency through the construction of optimized hollow ZnO/cu Mott-Schottky heterojunction microreactors, J. Alloys Compd. 1014 (2025) 178634, https://doi.org/10.1016/j.jallcom.2025.178634.
[63] L. Li, Y. Yu, S. Lin, W. Chu, D. Sun, Q. Su, S. Ma, G. Du, B. Xu, Single ruthenium atom supported on g-C_3N_4 as an efficient photocatalyst for nitrogen fixation in ultra-pure water, Catal. Commun. 153 (2021) 106294, https://doi.org/10.1016/j.catcom.2021.106294.
[64] Y. Xue, C. Ma, Q. Yang, X. Wang, S. An, X. Zhang, J. Tian, Construction of g-C_3N_4 with three coordinated nitrogen (N3C) vacancies for excellent photocatalytic activities of N2 fixation and H2O2 production, Chem. Eng. J. 457 (2023) 141146, https://doi.org/10.1016/j.cej.2022.141146.
[65] X. Gao, L. An, D. Qu, W. Jiang, Y. Chai, S. Sun, X. Liu, Z. Sun, Enhanced photocatalytic N2 fixation by promoting N_2 adsorption with a co-catalyst, Sci. Bull. 64 (2019) 918–925, https://doi.org/10.1016/j.scib.2019.05.009.
[66] R. Guan, D. Wang, Y. Zhang, C. Liu, W. Xu, J. Wang, Z. Zhao, M. Feng, Q. Shang, Z. Sun, Enhanced photocatalytic N_2 fixation via defective and fluoride modified TiO_2 surface, Appl. Catal. Environ. 282 (2021) 119580, https://doi.org/10.1016/j.apcatb.2020.119580.
[67] S. Wang, X. Hai, X. Ding, K. Chang, Y. Xiang, X. Meng, Z. Yang, H. Chen, J. Ye, Light-switchable oxygen vacancies in ultrafine Bi_5O_7Br nanotubes for boosting

solar-driven nitrogen fixation in pure water, Adv. Mater. 29 (2017) 1701774, https://doi.org/10.1002/adma.201701774.
[68] J. Li, Q. Li, Y. Chen, S. Lv, X. Liao, Y. Yao, Size effects of Ag nanoparticle for N_2 photofixation over Ag/g-C_3N_4: built-in electric fields determine photocatalytic performance, Colloids Surf. A Physicochem. Eng. Asp. 626 (2021) 127053, https://doi.org/10.1016/j.colsurfa.2021.127053.
[69] D. Li, Q. Li, Q. Zhang, R. Yang, Q. Ye, D. Tian, D. Jiang, Integrating bimetallic borides with g-C_3N_4 containing cyanamide defects for efficient photocatalytic nitrogen fixation, J. Colloid Interface Sci. 672 (2024) 631–641, https://doi.org/10.1016/j.jcis.2024.05.238.
[70] E. Dhanaraman, A. Verma, P. Anand, Y.-P. Fu, Influence of B-atom in g-C3N4 matrix to enhance the photocatalytic dinitrogen to ammonia conversion, J. Environ. Chem. Eng. 11 (2023) 111323, https://doi.org/10.1016/j.jece.2023.111323.
[71] H. Ma, Z. Shi, Q. Li, S. Li, Preparation of graphitic carbon nitride with large specific surface area and outstanding N_2 photofixation ability via a dissolve-regrowth process, J. Phys. Chem. Solid 99 (2016) 51–58, https://doi.org/10.1016/j.jpcs.2016.08.008.
[72] S. Ajmal, A. Rasheed, N.Q. Tran, X. Shao, Y. Hwang, V.Q. Bui, Y.D. Kim, J. Kim, H. Lee, Electron deficient boron-doped amorphous carbon nitride to uphill N2 photo-fixation through π back donation, Appl. Catal. Environ. 321 (2023) 122070, https://doi.org/10.1016/j.apcatb.2022.122070.
[73] T.N. Das, R.E. Huie, P. Neta, Reduction potentials of $SO_3^{\bullet-}$, $SO_5^{\bullet-}$, and $S_4O_6^{\bullet 3-}$ radicals in aqueous solution, J. Phys. Chem. A 103 (1999) 3581–3588, https://doi.org/10.1021/jp9900234.
[74] X. Gao, Y. Wen, D. Qu, L. An, S. Luan, W. Jiang, X. Zong, X. Liu, Z. Sun, Interference effect of alcohol on Nessler's reagent in photocatalytic nitrogen fixation, ACS Sustain. Chem. Eng. 6 (2018) 5342–5348, https://doi.org/10.1021/acssuschemeng.8b00110.
[75] H. Wei, Q. Zhang, Y. Zhang, Z. Yang, A. Zhu, D.D.D. ionysiou, Enhancement of the Cr(VI) adsorption and photocatalytic reduction activity of g-C_3N_4 by hydrothermal treatment in HNO3 aqueous solution, Appl. Catal. Gen. 521 (2016) 9–18, https://doi.org/10.1016/j.apcata.2015.11.005.
[76] X. Li, X. Sun, L. Zhang, S. Sun, W. Wang, Efficient photocatalytic fixation of N2 by KOH-treated g-C_3N_4, J. Mater. Chem. A 6 (2018) 3005–3011, https://doi.org/10.1039/c7ta09762j.
[77] G. Li, L. Li, H. Yuan, H. Wang, H. Zeng, J. Shi, Alkali-assisted mild aqueous exfoliation for single-layered and structure-preserved graphitic carbon nitride nanosheets, J. Colloid Interface Sci. 495 (2017) 19–26, https://doi.org/10.1016/j.jcis.2017.01.112.